Experimental study of the structure of a passive scalar in turbulent flows using a wire-mesh sensor: Pipe flow and rod-bundle axial flow

MSc Thesis

Delft University of Technology
Faculty of Applied Sciences

Department of Radiation Science and Technology
Section of Nuclear Energy and Radiation Applications

Department of Chemical Engineering
Section of Transport Phenomena

Author:
M. Buskermolen
Studentnumber:
1382489

Supervisors:
Dr. L. Portela
Dr. Ir. M. Rohde
Reviewers:
Prof. Dr. Ir. P. Kruit
Prof. Dr. R.F. Mudde

1st May 2014

Abstract

One of the vital safety mechanisms in the reactor core of most nuclear power plants is the negative feedback from the core temperature on the power output. An increased temperature will reduce the power output of the reactor, 'automatically' cooling the it and preventing the nuclear reaction to spin out of control. For this reason, it is important to have a good understanding of the temperature distribution within the reactor core. The water that flows through the core is the main reason for the transport of heat, hence it is of interest to have a good understanding of the behavior of the flow. On of the aspects that defines the flow properties is the geometry of the reactor, a so called 'rod-bundle geometry'. It is the presumption that a large shear in the fluid, induced by the geometry, causes the formation of large-scale coherent structures. These structures affect the mixing of heat in the reactor and are, therefore, of interest.

In this research, the existence of these structures is examined with passive-scalar measurements using a wire-mesh sensor. This sensor is a conductivity-based sensor that is able to determine the local conductivity in the entire cross-section of the flow-geometry, without the need for optical access.

Passive-scalar measurements in single-phase flow is a relatively new application of the wire-mesh sensor. In this research, the measurement technique is improved. Primarily, the variance in statistical flow-properties like correlation functions and spectral densities was reduced.

To determine the reliability of the data from the wire-mesh sensor measurements were done in a pipe flow experiment at the Reynolds numbers 18 000 and 41 000. The results were compared with previous studies. Furthermore some interesting data about the structure of a passive scalar in the center of a turbulent pipe flow was found.

The experiment on the existence of large-scale coherent structures was done in vertical, gravitational driven, rod-bundle geometry, that consisted of 3 x 3 subchannels, who were connected by a gap. The pitch-to-diameter ratio of the rods was 1.4 and the experiment was performed at the Reynolds numbers 750, 1500, 3000, 4500 and 6000. Two kind of structures were found: Structures with a size in the order of the hydraulic diameter of the geometry, which were present in laminar flow, and structures with a size in the order of 10 hydraulic diameters, which were present in the turbulent flows.

This research was realized as a collaboration between the sections Nuclear Energy and Radiation Applications (NERA) and Transport Phenomena (TP) of the faculty of Applied Sciences from the Delft University of Technology.

Samenvatting

Een van de essentiele veiligheidsmechanismen van de reactor kern van de meest kerncentrales is de negatieve terugkoppeling van de temperatuur op het vermogen van de reactor. Een hogere temperatuur leidt tot een vermindering van het vermogen van de kerncentrale, waardoor de reactor 'vanzelf' weer afkoelt. Dit zorgt er dus voor dat de nucleare reactie niet oncontroleerbaar wordt. Daarom is het belangrijk om goed te begrijpen hoe de warmte verdeling binnen een reactor kern plaatsvindt. Het water dat door een reactor stroomt is de voornaamste oorzaak van warmte transport binnen the kern, dus het is belangrijk om goede kennis te hebben over de eigenschappen van de stroming. Een van de aspecten die de stromingseigenschappen bepaald is de geometrie van de reactor kern, de zogenaamde 'rod-bundle' geometrie. Het wordt aangenomen dat er een grote schuifkracht in de vloeistof bestaat, veroorzaakt door de geometrie, die zorgt voor de formatie van grote coherente structuren. Deze structuren kunnen het mengen van warmte door de reactor beïnvloeden.
In dit onderzoek wordt het bestaan van deze structuren onderzocht door het meten van een passieve scalar met een wire-mesh sensor. Deze kan de lokale conductiviteit van een vloeistof in de gehele doorsnede van de geometrie meten, zonder dat daar visuele toegang voor nodig is.
Het meten van een passieve scalar is een relatief nieuwe toepassing van de wire-mesh sensor. Daarom was het nodig om een aantal verbeteringen in de meettechniek aan te brengen. Vooral in statische eigenschappen zoals correlatie functies en power spectra zat een zeer grote variantie.
Om de betrouwbaarheid van de metingen te valideren is een experiment in een pijp stroming gedaan bij de Reynolds getallen 18 000 en 41 000. De resultaten zijn vergelijk met onderzoeken uit de literatuur. Verder is nog interessante data gevonden over de turbulente structuren in het midden van de pijp stroming.
Het experiment om grote coherente structuren te vinden is gedaan in een vertikale, zwaartekracht aangedreven rod-bundle geometrie die bestond uit 3 x 3 subkanalen, die aan elkaar verbonden waren via smalle openingen. De verhouding van de hartsafstand tot de diameter was 1,4 en het experiment is gedaan bij de Reynolds getallen 750, 1500, 3000, 4500 en 6000. Twee soorten structuren zijn gevonden gevonden, structuren met een grootte in de orde van de hydraulische diameter, die in laminaire stromingen voorkwamen en structuren met een grootte in de orde van 10 hydraulische diameters, die in turbulente stromingen voorkwamen.

Dit onderzoek is gerealiseerd via een samenwerking tussen de secties Nuclear Energy and Radiation Applications (NERA) and Transport Phenomena (TP) aan de faculteit voor Technische NatuurWetenschappen (TNW) aan de TU Delft.

Contents

Chapter 1

Introduction

The physics of flows is one of the most investigated subjects in the field of applied physics. Due to the extensive use of flows in different industries for the transport of mass and heat, this field of research tends to be very close to application outside the laboratory environment. For the research of flows several techniques exist, such as 'hot wire anemometry (HWA)', 'particle image velocimetry (PIV)' and 'laser doppler anemometry (LDA)'. In this research, a recent technique to measure statistical properties with the wire-mesh sensor is further developed. This sensor has some features which makes it an interesting tool in fluid dynamics. For example, there is no optical access needed, and it consists of multiple probes, so measurements in a complete cross sectional plane in a flow geometry can be done simultaneously. This features the possibility to do measurements in complex geometries, where the use of lasers is difficult. The principle of the sensor is measuring the local electrical conductivity at the intersections in a grid of stainless steel wires. This makes it a suitable sensor for passive-scalar measurement.
In this research the technique of passive-scalar measurement with a wire-mesh sensor is improved. Next, the technique is applied to a pipe flow, to determine the scalar spectral density and to examine the existence of large-scale structures. Furthermore, measurements are done in a 'rod-bundle axial flow', to investigate the existence of large-scale coherent structures as a next step in improving the mixing properties of this geometry.

1.1 Rod-bundle geometry

The rod-bundle geometry is a flow geometry that consists of a flow in the axial direction through an array of rods as in figure 1.1a. This geometry is often used in heat exchangers, because of the large contact surface between the rods and the flow. The array of rods forms a set of channels where the fluid flows through. Each of these channels a called a 'subchannel'. Since the rods are not closely packed, there is a small space between two adjacent rods, connecting each subchannel with its neighbor. These connections are called 'gaps'. In figure 1.1b a schematic drawing of these subchannels and gaps can be seen.
The rod-bundle axial flow has a complex three dimensional structure. The fluid flows through the subchannels in the streamwise direction. The gaps connecting the subchannels create the possibility of a net flow in the lateral direction from one subchannel to another. Because the width of the gap is much narrower than the subchannel, the streamwise velocity will be lower. This could give rise to a large shear-stress at the interface of the fluid flowing in the gap and the fluid in the subchannels. This large shear-stress can cause the formation of large coherent vortices, as in figure 1.1c, which affect the mixing properties of the flow. In a geometry that is most often used in heat exchangers the mixing properties are of great interest.
The complex geometry makes it difficult to access it with commonly used experimental techniques. For example, measurements with lasers are very complicated, because of refraction by the rods. Although

there has been done a lot of research in the past to the existence of these coherent vortices, the results were inconclusive and the discussion is ongoing. In this research, a contribution is made using an innovative measurement technique.

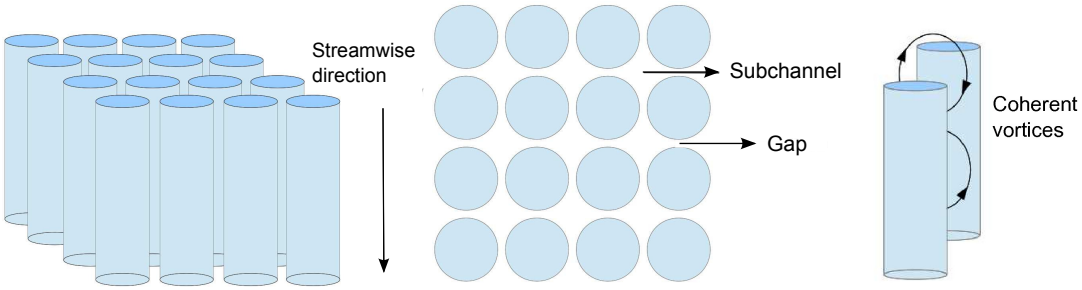

(a) The front view of a rod-bundle geometry

(b) Top view of a rod-bundle geometry

(c) Coherent vortices in a rod-bundle geometry

Figure 1.1: The rod-bundle geometry consists of an array of rods where the fluid flows through. At the interface between the subchannel and the gap coherent vortices can form.

1.2 Nuclear reactors

There are over 400 nuclear power plants in the world operational. Most of them use fission of uranium as a heat source to produce steam, which powers a turbine. In these reactors, the nuclear fuel is kept in a reactor vessel, where it is arranged in an big array of fuel rods, forming a rod-bundle geometry. The steam is produced by pumping water through the rod-bundle of fuel rod. In figure 1.2 an element of the fuel rod assembly in a 'Pressurized Water Reactor (PWR)' is visible as an example.
The properties of the nuclear fuel dependent among others on the temperature. Part of the safety of a reactor is based on a negative feedback system of the operating temperature of the reactor. In a well designed reactor, the power of the reactor is dependent of the temperature such that if the temperature goes up, the power goes down, cooling the reactor to its normal operating temperature 'automatically'. The mixing properties of the rod-bundle geometry can play a major role in distributing the heat of the fuel evenly throughout the reactor core. Because of the temperature dependency of the reactor, a better distribution of heat in the reactor can improve the controllability and inherent safety of a reactor. The earlier mentioned large-scale coherent vortices could improve the mixing in a rod-bundle. It is therefore important to get a better understanding of this phenomenon. More about coherent vortices can be read in section 5.1.

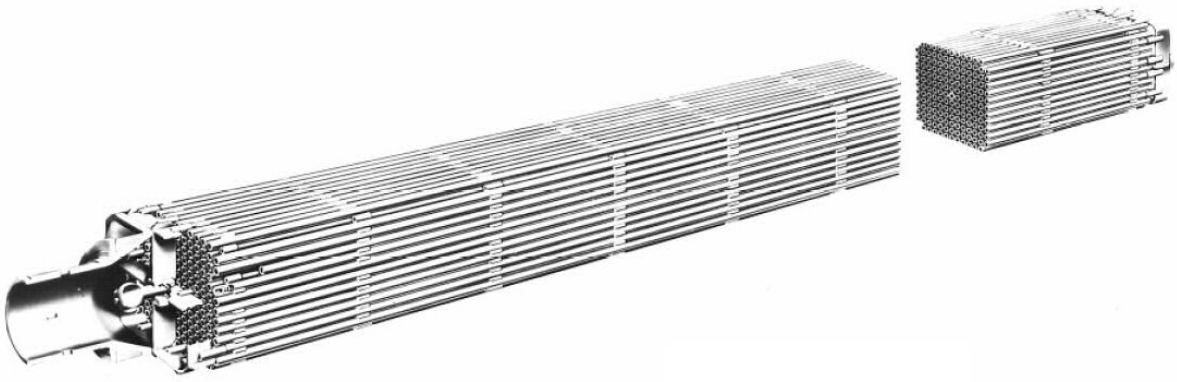

Figure 1.2: A part of the array of fuel rods from the PWR of the ship NS Savannah. Source: U.S. Maritime Administration.

1.3 Previous work

Due to the significant effect that the flow properties of a rod-bundle can have on the safety and stability of a nuclear power plant, a lot of research has been done in the past. In the sixties, researchers like Coates [1] and Rogers and Todreas [2] were among of the first to examine the mixing mechanism in the actual fuel elements. Their focus was mainly of the forced mixing caused by the spacers that keep the fuel rods together. After them, Rowe [3] did experiment on the mixing properties caused by the flow geometry itself. He found that the rod gap spacing (pitch-to-diameter ratio) is the most significant geometric parameter affecting the flow structure'. In 1992, Rehme [4] made a review paper on the existing experimental data from which he concluded that 'the almost periodical flow pulsation between subchannels are the main reason for the natural mixing between subchannels of rod-bundles'.

At TU Delft, Mahmood [5] has done research on the mechanism of the formation of vortices. In different geometries numerical simulations were performed and measurements were done with both PIV and LDA. Van Campen [6] also did research on rod-bundle flows, using LDA and refractive index matching. They both found the existence of coherent structures at the interface of the gap region and the subchannel. Furthermore, they concluded that the structure size is inversely dependent on the Reynolds number. Ylönen [7] was the first to use the wire-mesh sensor for passive-scalar measurement, in a rod-bundle geometry. He successfully performed dispersion measurements and made probability density functions from the measured times-series. These studies were followed by the work of Bulk [8], who was the first to use a wire mesh sensor in a rod-bundle axial flow at the TU Delft. He found indications of the presence of coherent structures in the flow by making correlation functions of his measurements.

passive-scalar measurement is a widely used technique to study the behavior of mixing and the structure of turbulence. It is thought that when introducing a passive-scalar gradient in the flow, like temperature or concentration, this scalar will be advected by the velocity field and will follow the structures in the flow. By measuring the scalar fluctuations, information about the flow structure can be extracted. It is found that the Schmidt (or Prandtl) number plays a vital role in the mechanism of the transport and mixing of the scalar through the flow. More information about the physics behind passive-scalar measurement can be found in section 2.4.

1.4 Objectives of this research

This research mainly focuses on continuing the work of Bulk. For this, the passive-scalar measurement technique with the wire-mesh sensor is improved. It was found necessary to confirm the measurements of the wire-mesh sensor and to check the quality of the data. For this purpose, measurements in a pipe flow were performed. Since pipe flow is extensively studied, plenty of literature is available to check the results of the wire-mesh sensor. In the pipe flow measurements of Reynolds number 41 000 and 18 000 were done. Besides a check of the measurement technique with the wire-mesh sensor, the physics of the pipe flow at these particular Reynolds numbers is examined. Furthermore, measurements in a rod-bundle axial flow were performed at Reynolds numbers varying from 750 to 6000.

In this thesis the following subjects are treated. In chapter 2, some theory about turbulence and passive-scalar measurement is presented. In chapter 3, information about the wire mesh sensor can be found. Chapter 4 and 5 contain a presentation and discussion of the measurement results of, respectively, the pipe flow and the rod-bundle axial flow. The finalizing conclusions and recommendations for further work can be found in chapter 6 and 7.

Chapter 2

Turbulent flow and mixing theory

Turbulent flows are one of the most extensive studied phenomena in fluid dynamics. Since the Navier-Stokes momentum equations, which describe the motion of a fluid, are non-linear, it is yet impossible to construct analytic solutions. Therefore, problems have to be solved by dimensional analysis, physical modeling and statistical descriptions. In this chapter, some fundamental characteristics for turbulent flows will be discussed. After this some information on the behavior of passive scalars in turbulent flows will be provided.

2.1 Isotropic turbulence

It is difficult to give a comprehensive definition of turbulence. Commonly used books in the field of fluid dynamics, like Kundu [9], attempt to characterize it as follows:

i. Chaotic: the motions in a turbulent seem to have random behavior. When one takes a closer look, it can be observed that a certain predictability within a certain time horizon exists.

ii. Non-linearity: this causes unstable behavior of motions in the fluid

iii. High diffusivity: motions in the large scale, cause a high rate of diffusion of mass and heat at the small scales

iv. Coherent structures with swirling motions, called eddies

v. Dissipation: the motions in the fluid dissipate the kinetic energy

In short, this means that the non-linear behavior of the fluid causes instabilities to grow. This creates a velocity field in the flow that seems to be random, but is not totally random. Swirls, called eddies, of different length scales cause mixing in the flow and eventually dissipate kinetic energy. The origin of the instabilities is when the inertial forces in the flow exceed the viscous forces. The ratio between the two is given by the Reynolds number, according to equation 2.1:

$$Re = \frac{U_{av} D_h}{\nu} \tag{2.1}$$

In this dimensionless number, U_{av} is the average mean velocity across the diameter of the flow-geometry. D_h is the hydraulic diameter and ν is the kinematic viscosity of the fluid.
Since, as mentioned before, it is impossible to solve a turbulent flow analytically, a more simplified approach is needed. The first step in this is to split the velocity components U, V and W in a mean part and a fluctuating part, as shown in equations 2.2

$$U = \overline{U} + u', \qquad V = \overline{V} + v', \qquad W = \overline{W} + w' \tag{2.2}$$

In these equations, the bar represents the mean component whereas the accent represents the fluctuating component. From these decomposed velocity components, the RANS (Reynolds-Averaged Navier-Stokes) equations (2.3) can be derived.

$$\frac{\partial \overline{U_i}}{\partial t} + \overline{U_j}\frac{\partial \overline{U_i}}{\partial X_j} = -\frac{1}{\rho}\frac{\partial \overline{P}}{\partial X_i} + \nu\frac{\partial^2 \overline{U_i}}{\partial X_i X_j} - \frac{\partial \overline{u_i' u_j'}}{\partial X_i} \tag{2.3}$$

In the RANS equations, the Reynolds stress tensor, $\overline{u_i' u_j'}$ becomes visible. The Reynolds stresses originate from the rate of mean momentum transfer by the turbulent fluctuations in the velocity field. Usually these stresses are much bigger than the viscous stresses, with exception the situation were a fluid particle is close to the wall or a solid body. In the case of isotropic turbulence, the flow statistics are invariant under any rotation of our frame of reference. Hence, all off diagonal components in the Reynolds stress tensor, i $\neq$ j, are 0, and $\overline{u'}^2 = \overline{v'}^2 = \overline{w'}^2$.

Scaling

Turbulent flows can be described in different scales. A famous model to define the scales and their interaction is the eddy-cascade model. In this model it is assumed that large eddies are formed at the macro-scale ℓ_0 (usually defined as the hydraulic diameter D_h; the actual largest motions can be several times D_h) by instabilities in the flow, this scale is called the energy-containing range. The eddies break up in smaller and smaller eddies until they reach the Kolmogorov scale ℓ_η, defined in equation 2.4:

$$\eta \equiv \left(\frac{\nu^3}{\epsilon}\right)^{\frac{1}{4}} \tag{2.4}$$

In this equation, ϵ is the dissipation rate. For ϵ various estimates exist, which will not be discussed now, but can be found in books like Kundu [9] or Pope [10]. At the Kolmogorov scale there is no longer the breaking-up of eddies, but instead they are dissipated by viscous forces. In order to go from the energy-containing range to the dissipation at the Kolmogorov scale, the energy must be transferred. This happens in the intermediate range, called the inertial subrange. We define this this range as $\ell_{DI} < \ell < \ell_{EI}$, as in the book of Pope [10]. The suffixes DI and EI indicate the demarcation lines between the Dissipation range, the Inertial subrange and Energy-containing range. There is no strict boundary between the three different scales, but we define them as $\ell_{EI} \approx \frac{1}{6}\ell_0$ and $\ell_{DI} \approx 60\eta$. An overview of the energy scales can be seen in figure 2.1.

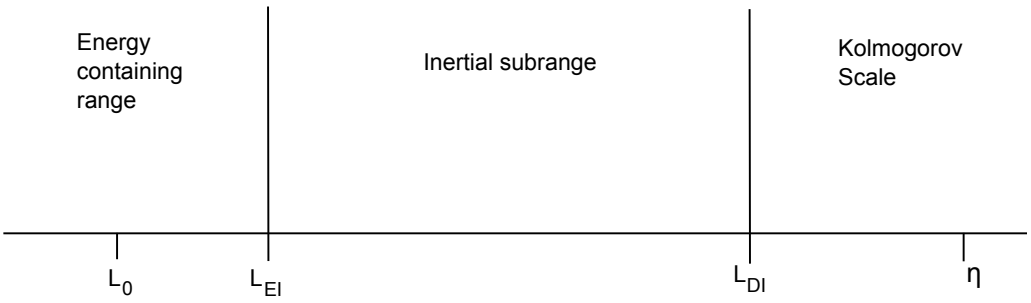

Figure 2.1: A schematic drawing of the scales in a turbulent flow

The $-\frac{5}{3}$ law

In pure isotropic turbulence, the energy spectrum shows a $\kappa^{-\frac{5}{3}}$ dependency in the energy spectrum, in which κ is the wave-number as defined in equation 2.5, at the length scales of the inertial subrange. This curve is the footprint of the break-up of eddies from the eddy-cascade model. This dependency can be analytically derived using the Kolomogorov hypotheses. The exact derivation according to the book of Pope [10] can be found in appendix A.

$$\kappa = \frac{2\pi}{\ell} \tag{2.5}$$

Turbulence structures
The velocity field of a turbulent flow is highly variable, with velocities varying in all directions. However, although it seems that all the motions are totally random, there can be a certain order in it. This order, or pattern in the flow is called a turbulence structure. The most common form of these structures is the eddy. This swirling motion may be the most common turbulence structure, but certainly is not the only one. Especially near walls structure-like patterns of different forms and sizes are found. These structures introduce a certain predictability over a certain time period in the velocity field and can therefore be of interest to characterize a flow. For example, in weather forecasting this is used to predict the motions of different pressure systems. Besides this, structure-like motions affect the mixing properties of the flow, which also can be of use in different applications.

2.2 Wall-bounded flows

True isotropic turbulence only applies to very high Reynolds numbers (in the order of hundreds of thousands) and very far from any wall. Usually these conditions can only be found in natural systems, like the ocean or the atmosphere. Under laboratory conditions, one always has to take into account the effect of the wall. This has some important consequences. To start with, there are all the different layers close to the wall, in which other mechanisms can be dominant for the behavior of the fluid. Furthermore, the eddy-cascade model applies very well to pure isotropic turbulence, but is an idealized model for wall bounded flows. The $-\frac{5}{3}$ law for the inertial subrange, does not necessarily have to be found in the energy spectrum of a wall-bounded flow. Therefore, in practice a flow can be made that is approximately isotropically turbulent, however never perfectly.

2.2.1 Large-scale structures

A characteristic of wall-bounded flows is the existence of coherent structures in the velocity field which do not exist in isotropic turbulence. As already discussed in the previous section, in turbulent flows there exist certain regularities in the velocity field called structures. Whereas in pure isotropic turbulence the eddy is the main structure, wall-bounded flows give rise to a whole spectrum of other turbulence structures. One family of structures, the very large structures in pipe flow, was extensively studied by Adrian et al. [11] [12] [13] [14]. In several studies, with both experiments and numerical methods, he proves the existence of large structures in the form of elongated velocity fluctuations in the streamwise direction. These structures have length scales of more than 10 times the pipe radius and form at high Reynolds numbers. In figure 2.2, the signature of the large structures in the pre-multiplied velocity spectrum can be seen. They appear in the pre-multiplied power spectrum as an easy notable peak at low wave-numbers.

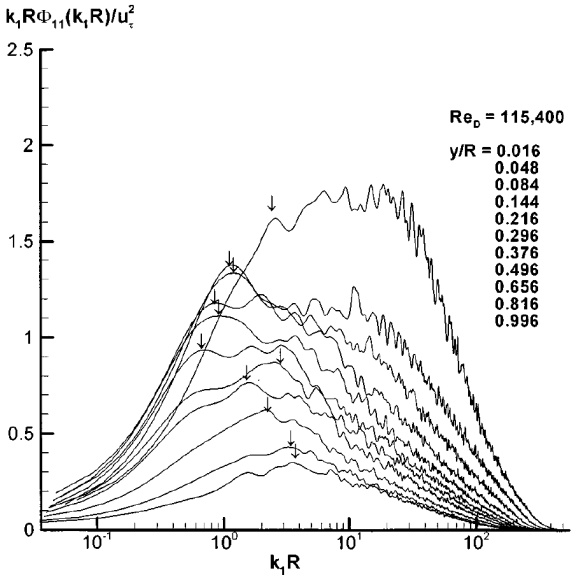

Figure 2.2: Pre-multiplied one-dimensional velocity spectra as function of the distance from the wall. Each arrow indicates the wave-number of the very-large-scale motion, $^{2\pi}/_{\Lambda_{max}}$; measurements by Adrian [11].

2.3 Taylor's hypothesis

In order to measure velocity spectra with a single probe, Taylor's hypothesis, also known as 'the frozen-turbulence approximation' can be used. In this hypothesis, it is assumed that the velocity field does not change over small time scales, while the mean velocity component advects the fluid past a

probe. This is also known as 'frozen field turbulence' and the implication is that it is possible to convert time-series for small enough timescales into spatial-series. The mathematical description of Taylor's hypothesis can be seen in equation 2.6:

$$\frac{\partial}{\partial t} = \overline{U}\frac{\partial}{\partial x} \tag{2.6}$$

This equation states that by using the transformation $x = \overline{U}t$, the measured time can be interpreted as a distance.
Depending on the properties of the flow, Taylor's hypothesis holds. First, the flow needs to be statistically stationary. Second, the mean streamwise velocity $\overline{U}$ needs to be large enough. Third, the hypothesis only applies to small times scales.
Summarizing, the eddies in the flow are advected by the mean flow so fast, that the eddies have no time to change while passing the probe. As a consequence, the measured time can be transformed into a distance.

2.4 Passive-scalar measurement

Injecting a passive scalar in a flow can provide information about the structure of the flow. The influence of a passive scalars on the flow structure can be neglected, therefore passive scalars can be used as a tracer. Well known examples of passive scalars are temperature- and concentration variations.
The injection of a passive scalar creates a gradient of that scalar in the flow and as a consequence the scalar will be mixed while being transported by the flow, as described by the scalar transport equation 2.7.

$$\frac{\partial C}{\partial t} + U_j\frac{\partial C}{\partial X_j} = \mathcal{D}\frac{\partial^2 C}{\partial X_j^2} \tag{2.7}$$

In this equation $C(\mathbf{x}, t)$ can be any scalar and $\mathcal{D}$ is the diffusion coefficient of the scalar in the fluid. Just like the velocity, C can be decomposed in a mean and a fluctuating part, so $C = \overline{C} + c'$.

In the large-scale and the inertial subrange, the dominating effect in the transport of the passive scalar is the advective term. The mixing of the passive scalar in the flow is mainly determined by the motions of the fluid, viscosity and diffusion play no role here. As a consequence, there exists an analogy between the fluctuating part of the scalar, c', and the fluctuations in the velocity. By examining the scalar fluctuations statistical properties of the flow like the power spectral density and correlation functions can be constructed. Fulachier and Dumas [15] concluded from experiments that this analogy approximately holds, although a shift in the frequency spectra can appear under certain conditions. It must be noted that although there exists a certain analogy between the fluctuations of a passive scalar and the fluctuations of the velocity, they are not the same.

2.4.1 Schmidt number dependency

A possible influence of the the behavior of the scalar is the ratio between the diffusion of momentum and the diffusion of mass. This ratio is represented by the Schmidt number, defined by equation 2.8.

$$Sc = \frac{\nu}{\mathcal{D}} \tag{2.8}$$

Batchelor [16] did a theoretical study on the influence of the Schmidt number on the variance spectra of passive scalars. He concluded that passive scalars in isotropic turbulence will behave like the eddy-cascade model. From the large-scale, the break-up of eddies will go through an inertial subrange. Here the variance spectrum will follow a curve according to $E(\kappa) = \kappa^{-\frac{5}{3}}$ for true isotropic turbulence. Eventually, the Kolmogorov length scale (κ_K) is reached. Here, the viscous forces become dominant, which causes the eddies to dissipate energy and die out. However, the scalar is able to mix up to the molecular level, so measurements of even smaller length scales can be done. Batchelor states that for $Sc \gg 1$ and length scales between the Kolmogorov- and the Batchelor lengthscale ($\kappa_B = \kappa_K Sc^{\frac{1}{2}}$) any distortion of a fluid particle is due to straining motions. From this, he concludes that the scalar-variance spectrum will follow a curve according to $\Gamma(\kappa) = \kappa^{-1}$ between the Kolmogorov- and the Batcholor length scale (κ_B), as can be seen in figure 2.3.

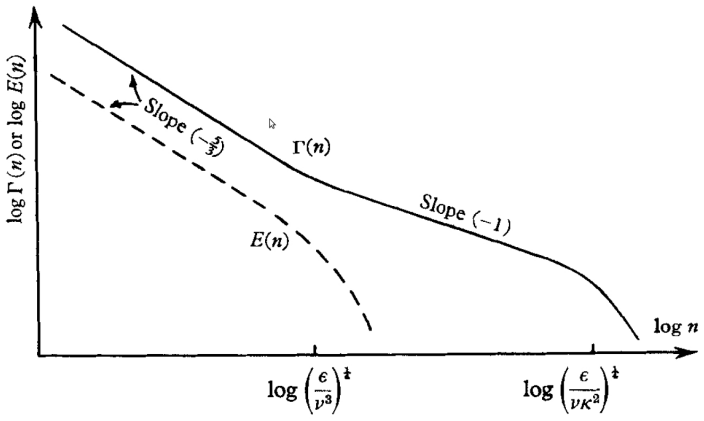

Figure 2.3: The variance spectrum for the velocity and for a passive scalar with $Sc \gg 1$, from Batchelor [16].

2.4.2 Taylor's theory of turbulent dispersion

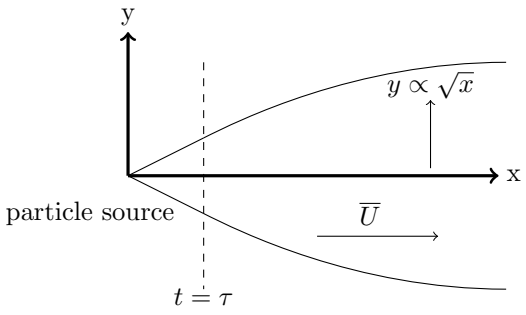

Figure 2.4: A plume of matter will disperse in a parabolic manner far from a source and in a linear manner close to the source.

The passive scalar that is injected in the flow will disperse over time. To describe this dispersion process Taylor came up with a model of a point source emitting particles. The particles start to perform a random walk, diffusing in the fluid. Taylor derived in his model that the average displacement of the particles from their source, the mixing rate, is dependent of two different timescales:

$$X_\alpha^{rms} = u_\alpha^{rms} t \qquad t \ll \mathcal{T} \tag{2.9a}$$

$$X_\alpha^{rms} = u_\alpha^{rms} \sqrt{2\mathcal{T}t} \qquad t \gg \mathcal{T} \tag{2.9b}$$

In equation 2.9 X_α^{rms} is the average displacement of a particle α, u_α^{rms} is the velocity of particle α and $\mathcal{T}$ the integral timescale of the flow. For small times, the intensity of the velocity fluctuations will be the dominant factor and the particle will move a distance $X = u\,\delta t$ for every time-step δt. Equation 2.9a is a direct consequence of the correlation between the displacement of the particles for small time steps with their previous position. For large timescale the correlation in the flow decreases to zero, the particles 'forget' their initial state at $t = 0$ and they get a $\sqrt{t}$ dependency. This is typical for a random walk.

When there is a mean velocity component in the flow, the particles will be advected while they disperse, this will create a plume of matter in which the different time-scales can be distinguished. While the particles are advected over a distance $x = U \cdot t$, the average dispersion in the y direction will be $y \propto \sqrt{x}$, resulting in a parabolic plume. Close to the source, the plume broadens linearly, a representation of this can be found in figure 2.4.

Chapter 3

Wire-mesh sensor

The wire-mesh sensor is a relative new measurement technique in the field of fluid dynamics that was mainly developed by Horst-Michael Prasser. In this chapter, the theoretical and historical background of the wire-mesh is treated. A description of the technical details of the wire-mesh is provided in section 3.1. In section 3.2 more about the experiments with the wire-mesh sensor in the past can be found. Section 3.3 provides some insights in the measurement of passive scalars using the wire-mesh sensor.

3.1 Technical details

The wire-mesh sensor is based on conductivity measurement. It consists of two planes with a number of parallel thin wires, which are rotated 90° with respect to each other. The planes are placed a small distance apart. One plane of wires contains the 'transmitting' wires, the other the 'receiving' wires. A small electrical potential is applied to the transmitting wires and then the current to the receiving wires is measured. From this, the conductivity at every crossing point of two wires can be determined. This gives a picture of conductivity throughout a plane in the flow.

Measurement procedure in detail
The wire-mesh sensors used in the study have a 32x32 grid of wires. Every grid-point functions as a probe for conductivity. By doing a sweep over all probes in a single measurement, the probes can be used as pixels in a plane, and pictures of the local conductivity in a plane can be determined. The resolution of this picture is the spacing of the wires, typically between 2 and 3 mm. A measurement sweep across all wires goes as follows:

i. A voltage is applied to one transmitting wire

ii. The current to all receiving wires is measured one by one

iii. The conductivity is determined, digitized and stored as an arbitrary 12-bit number

iv. A voltage is applied to the next transmitting wire

This procedure is visualized by the scheme of the wire-mesh made by Prasser [17] shown in figure 3.1.

Electronic issues
A DC current through water can cause electrolysis. Since this is can potentially disrupt the flow and influence the measurement, this has to be prevented. Prasser [17] solved this problem by applying a square pulse with a positive and negative component of equal length and amplitude to drive the transmitting wires. In traditional sensors, a sine-shaped pulse is used, this has a side effect that changes in the conductivity modulated the measured current, so demodulation is required. When using the square

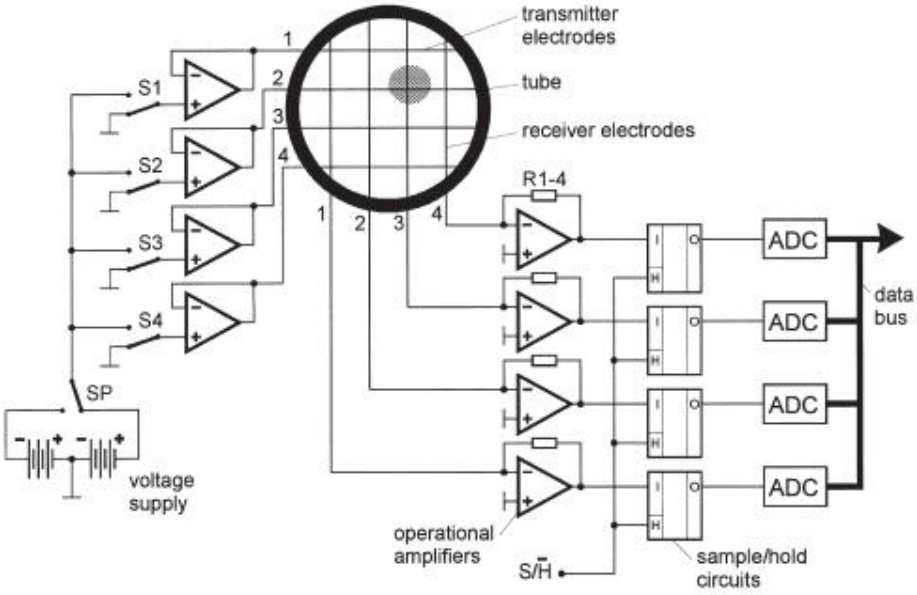

Figure 3.1: The original scheme of the wire-mesh as designed by Prasser [17]

pulse, the current first suffers from some transient behavior, caused by the capacitance effect from the ions in the fluid and the capacitance of the cable. When steady-state is reached, the current can be read out directly, making for demodulation of the signal unnecessary.
Another undesirable effect is so called cross-talk. A phenomena which can happen when a current from an activated transmitter wire flows to a non-activated transmitter wire. This can cause a non-zero potential of this wire, which can cause a current to a receiving wire. This gives false results and leads to blurring of the measurement. To prevent for cross-talk, both the drivers for the transmitting output and the receiver inputs were designed with a much lower impedance than the fluid. This guarantees that none of the potentials from the wires will deviate from zero.

Probe size
The wire-mesh sensor generates pictures with the local conductivity in a plane. The pixels in this picture, however, are not square and slightly overlap. Smeets [18] did a numerical calculation of the measurement volume. He found that, because of the shape of the electrical field, the pixels have a slightly diamond shaped form, as can be seen in figure 3.2. This can have consequences for the size of the probe. When measuring a passive scalar this can be of importance, since the probe size represents the shortest wave length that can be measured. An ideal probe therefore has an infinitesimal small length. In this research, the smallest distance between a transmitting and a receiving wire was a chosen as the probe size. This is according to the findings of Walker [19], who used conductivity as a passive scalar in a single phase flow mixing experiment.

3.2 Experiments with the wire-mesh sensor

Since the wire-mesh was built by Prasser, it has been used in several studies, with varying applications. In 1998, the wire-mesh sensor was used in an experiment for the first time. It was used in gas-liquid multi-phase flows to visualize bubbles and to measure the gas fraction [17]. In following years, Prasser et al. used the wire-mesh for bubble size measurements [20] and the evolution of the bubble size distribution [21]. Furthermore, the wire-mesh sensor itself was made faster [22] and able to withstand higher temperatures and pressures [23]. After the initial experiments in multi-phase flows, studies in single-phase flows were performed by Walker et al. [19]. He investigated the mixing in T-junction geometries. The first steps into the use of passive scalars in combination with the wire-mesh sensor as done in this research, were done by Prasser in an attempt to reconstruct the velocity in a time-dependent flow [24]. In

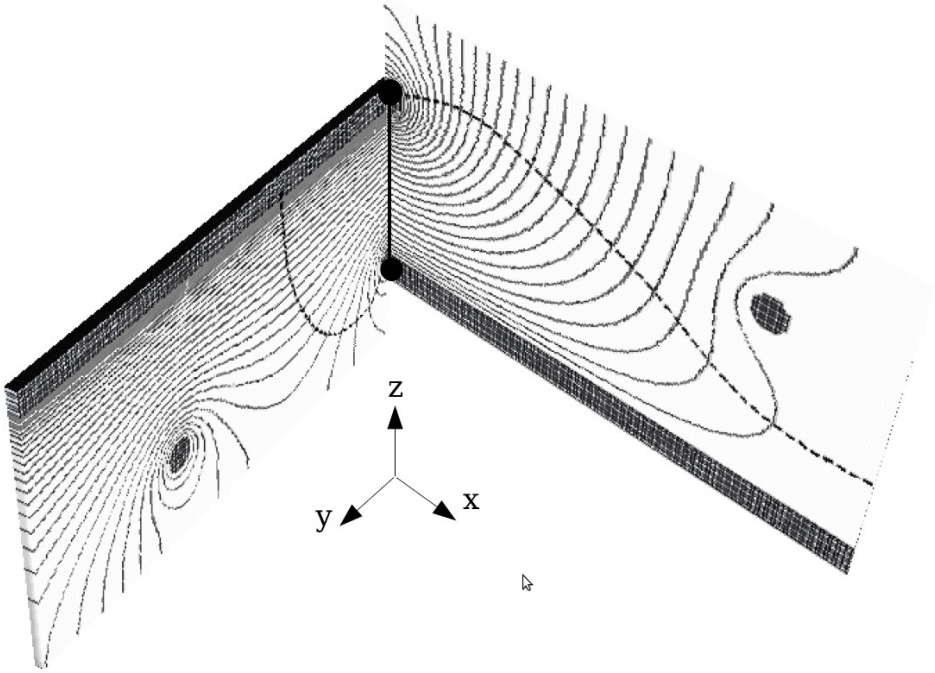

Figure 3.2: Equi-potential lines in the wire-mesh sensor as calculated by Smeets [18]. The dashed line represent the approximate measurement volume. On the left a transmitting wire can be seen and on the right side there is a receiving wire. A diamond shaped volume can be observed.

2011, Ylönen [7] used the wire-mesh sensor in a rod-bundle geometry in combination with passive-scalar injection to study the mixing in the flow.

At TU Delft the wire-mesh sensor technique has been used in different studies, with varying applications, including some new ones. In 2003 Manera [25] studied the behavior of flashing flows in a nuclear boiling water reactor (BWR). In her research, she used the wire-mesh sensor to measure the void fraction in the flow. In 2007, Descamps [26] studied, together with Smeets [18], three-phase flows in vertical pipes. The wire-mesh was used to determine the concentration of air, water and oil in the flow. Also in 2007, Belt [27] used an annular wire-mesh to determine the film thickness in annular flow. In 2012, Bulk [8] did his research on the existence of coherent structures in a rod-bundle geometry. He used the wire-mesh sensor to measure a passive scalar to study the coherent structures in the flow. In 2014, Van Campen [28] published his work on axial cyclones where he used a new type of wire-mesh sensor, the capacitance-based wire-mesh. He used this to distinguish oil droplets from salt water.

3.3 Passive scalars and the wire-mesh

In this study, a passive scalar is used as a tracer for the velocity fluctuations. As explained in section 2.4, it is possible to do determine statistical properties of the flow using the fluctuations of a scalar. The passive scalar is injected upstream in the flow with a small capillary in order not to disturb the flow. After injection, the passive scalar needs some development length, before properties like the spectral density no longer change shape when measuring further away from the injection point. The precise amount of development length needed depends on the type of passive scalar that is injected and on the fluid flow. From experiments in the pipe flow, it was found that 10 hydraulic diameters of development length are sufficient for the salt-water in the water flow used in this research.

3.3.1 Calibration

As an output, the wire-mesh gives 12-bit numbers without any unit, hence a calibration is necessary. In order to do this, a few difficulties in the behavior of the wire-mesh need to be mentioned. First, the diamond shape of the pixels treated in section 3.1 causes the center pixels to have a stronger response than the pixels near the wall. Second, the behavior of the wire-mesh is not strictly linear. Although a linear approximation works well for small deviations, over the entire measurement range it does not. Third, the data acquisition box causes behavior to a few of the wires which might be described as cross-talk. This is a malfunction in the data-box. These pixels will be excluded when evaluating the results.

Whereas in gas-liquid flows these difficulties are not a big problem, since there is such a high contrast in the conductivity of water and air, they do give problems in the measurement of salt-water in water. Figure 3.3 shows clearly that is is not very difficult to make a distinction between water and air in a multi-phase flow, but that it is a lot harder to make this distinction between tracer-fluid and plain water in the single-phase flow.

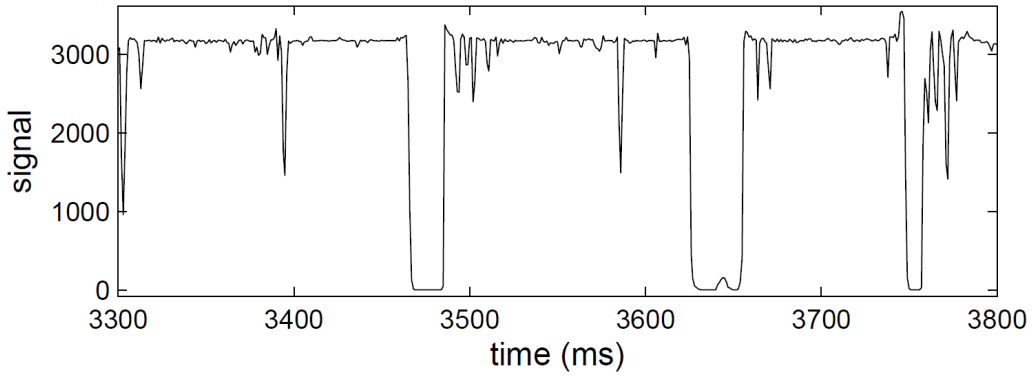

(a) Time-series of an arbitrary pixel in multi-phase flow, from Smeets [18].

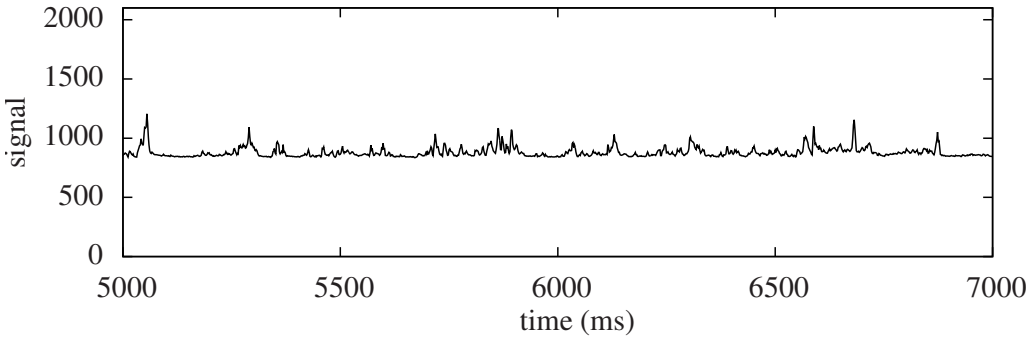

(b) Time-series of an arbitrary pixel from the measurement of a passive scalar in single phase flow

Figure 3.3: There is a lot more contrast in the measurement in multi-phase flow, (figure 3.3a), compared to passive-scalar measurement in single-phase flow, (figure 3.3b).

To calibrate the the wire-mesh, Ylönen [7] proposes the following formula:

$$\Theta_{i,j,k} = \frac{I_{i,j,k} - I_{demi,i,j}}{\frac{\gamma_{trac}}{\gamma_{ref,i,j}} I_{ref} - I_{demi,i,j}} \tag{3.1}$$

In this formula $I_{i,j,k}$ is an individually measured data-point k of pixel (i,j). $I_{demi,i,j}$ and $I_{ref,i,j}$ are the time-average at pixel (i,j) of a measurement in, respectively, demi-water and a reference fluid. Since the pure tracer fluid has a conductivity that is to high for the wire-mesh sensor to measure, a reference

fluid of a lower conductivity is used to calibrate. To compensate for this, a linear relationship in the conductivity is assumed, and the reference measurement is multiplied by the ratio of the conductivity of the tracer fluid γ_{trac} and the reference fluid γ_{ref}. This results in $\Theta_{i,j,k}$, the calibrated data-point k of pixel (i, j).
Although this is a nice calibration technique, it did not work for this research for two reasons. First, a lot of measurements were performed, which resulted in a small drift in the conductivity of the background. This is caused by the continuous injection of tracer-fluid and the warming-up of the water in the system, due to a pump. By using the method of Ylönen, this would result in the detection of a higher conductivity without the presence of more tracer fluid. Second, the error from the data-acquisition box was not constant over time, so a reference measurement would not be reliable. Hence it was necessary to make reference measurements regularly. To solve for these problems, it was decided to use a somewhat easier calibration:

$$\Theta_{i,j,k} = I_{i,j,k} - I_{background,i,j} \tag{3.2}$$

In which $I_{background,i,j}$ is the time-average of pixel (i, j) of a measurement of the bulk fluid in the system without tracer. This method allows one to calibrate the wire-mesh before every measurement. The downside is that it is not possible use the wire-mesh as a real conductivity probe, so it is impossible to determine the *absolute* conductivity. Instead, the distribution of *added* conductivity throughout a cross-section of the flow is measured. Since this research focuses on the statistical properties of the flow and this method will give the same fluctuations in the concentration, this is not a problem.

3.4 Data processing

When analyzing the time-series obtained with the wire-mesh sensor it can found that the variance in the statistical properties, like the power spectral density, of the flow is high. In order to reduce this, several techniques can be used.

A first step in reducing the variance in statistical properties is using the fact that the flow is in a statistically steady state. This means that for computing power spectra and correlation functions the results are statistically identical for any measurement. Therefore 'ensemble averaging' can be an easy solution to reduce the variance. By taking the average of the power spectrum or the correlation function for n time-series, the variance is reduced by a factor $\sqrt{n}$. The square-root makes this method of reducing the variance less effective when more measurements are done. To reduce the variance by a factor of two, four times more measurements are needed. Because the set-up used in this research could not do measurements autonomous, every measurements has to be started manually. This makes the effect of the method practical for up to 10 to 20 measurement series. After this, the amount of extra work that has to be done is not in proportion to the variance reduction that is achieved.

The ensemble averaging is enough to compute smooth correlation functions, but for constructing power spectral densities clever computation of the available data has to be done. For computing the power spectral density, roughly two families of methods are available. The parametric and the non-parametric models. Parametric models try to estimate a power spectrum by describing it a stationary stochastic system. Because this requires some knowledge about the spectrum in advance, we will limit ourselves to the non-parametric methods, which are 'safer' to work with.

The most simple estimator for the power spectral density is the periodogram, the absolute value of the Fourier transform of the time series. The periodogram actually is a very bad estimator for the spectral density, because in practice, it has a high variance. This variance can be reduced theoretically by taking longer time series, but even hundreds of thousands of data points are not sufficient to get a significant reduction. However, clever computation can reduce the variance significantly. One way is to improve the performance of the periodogram in estimating the true power spectrum is by reducing the spectral leakage. The 'leakage' of power from low to high frequencies. In order to reduce spectral leakage, the time-series can by multiplied by a data window D_n. A data-window is nothing more than a symmetric shaped function with the same length as the time-series. There are many kinds of window-functions, each with their own advantages and the corresponding disadvantages. The choice of a specific window always is a trade-off between properties like time- versus frequency-resolution. In practice this means that a

certain window can have a smoothing effect on a spectrum at the cost of a lower frequency-resolution. This means that sharp peaks in the spectrum will be no longer detectable.
The periodogram with the use of a window-function is called a modified- or extended periodogram. This periogram still has a high variance by definition, which only reduces for infinite samples. A solution can be a convolution with smoothing-function $G(\omega)$. This can be a simple moving-average filter, but also here various possibilities are present. Again, the price for using a smoothing function is loss of resolution in the spectrum. The resulting power spectral density becomes $\hat{S}(\omega)$ and can be computed as in equation 3.3:

$$\begin{aligned} S(\omega) &= \left| \sum_{n=1}^{n=N} x[n] D_n e^{-i\omega n} \right|^2 \\ \hat{S}(\omega) &= S(\omega) \star G(\omega) \end{aligned} \tag{3.3}$$

However, the variance in the periodogram is usually so high that it is impossible to say whether the resulting smoothed function is a good estimator.

When long measurement can be made, it is possible to use the Welch Overlapped Segment Averaging (WOSA) method, described in the book of Percival and Walden [29]. This method uses the same computation to estimate the power spectrum as the periodogram, but it makes better use of the existing data. The data is cut into pieces and for every piece a power spectrum is computed. Next the spectrum estimate is computed as the the average of all pieces. To prevent for spectral leakage both windowing and overlap in the data pieces is used. A visual representation of this can be found in figure 3.4. The measured time-series need to be long, because the cut pieces need to be longer than the lowest frequency, or longest timescale, present in the signal. Just like the periodogram, the resulting function can be convoluted with a smoothing function in order to smooth it.

An alternative to the WOSA method is the Thomson multitaper method. This method builds on the WOSA method and uses multiple orthogonal tapers, or window functions, in order to reduce the variance. However similar result to the WOSA method were obtained in this study, at significant higher computation times, so the WOSA method was chosen as an estimator for the power spectral density. More information on the multitaper method can be found in the book of Percival and Walden or the paper of Thomson [30].

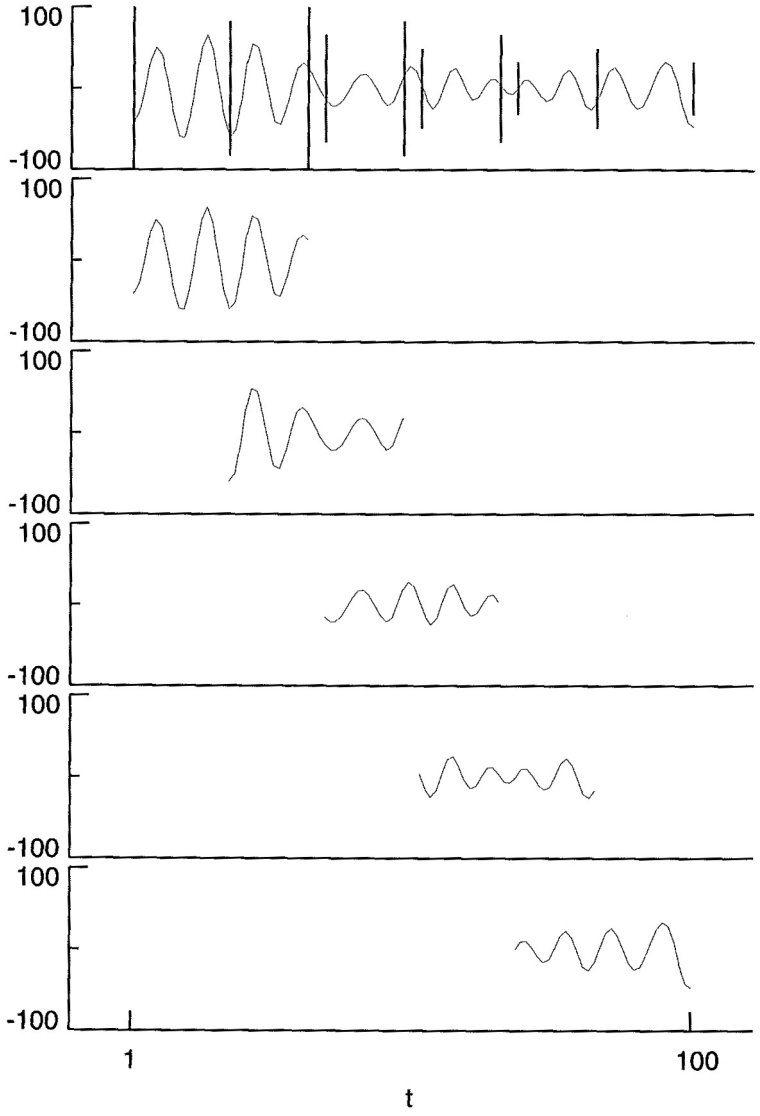

Figure 3.4: A visualization of the breaking-up of a time-series in overlapping pieces in order to estimate the power spectrum, from Percival and Walden [29].

Chapter 4

Pipe flow

The flow through a pipe is one the most extensively studied flow geometries in the field of fluid dynamics. The geometry is easy to describe mathematically and is one of the few problems in turbulence where some (simplified) analytic solutions are possible. Furthermore this geometry is easy to construct and has a lot applications outside the laboratory environment. Because of the abundance of information on the physics of pipe flow in literature, this geometry was chosen to test and optimize the passive-scalar measurement with a wire-mesh sensor. The results could be compared with the work of other researches and checked to determine whether they are reliable. This gives a certain reliability on the quality of other measurements with a wire-mesh sensor. The measurements from the pipe flow can be used for comparison with the rod-bundle geometry. The differences and/or similarities between the pipe flow and the rod-bundle axial flow can be used in the construction of a mixing model for the rod-bundle geometry.

4.1 Experimental set-up

The set-up used is a gravity-driven horizontal pipe flow, with an inner diameter of 10 cm and a development length of about 300 diameters. The driving-pressure is obtained from the main-reservoir placed above the pipe. The water is kept in the flow system and flows from the main-reservoir through the pipe to a buffer-reservoir, from which it is pumped back into the main-reservoir with an electric pump. The electric pump is switched on and off by an ultrasound height-sensor above the buffer-reservoir, keeping the water level, hence the pressure, constant.

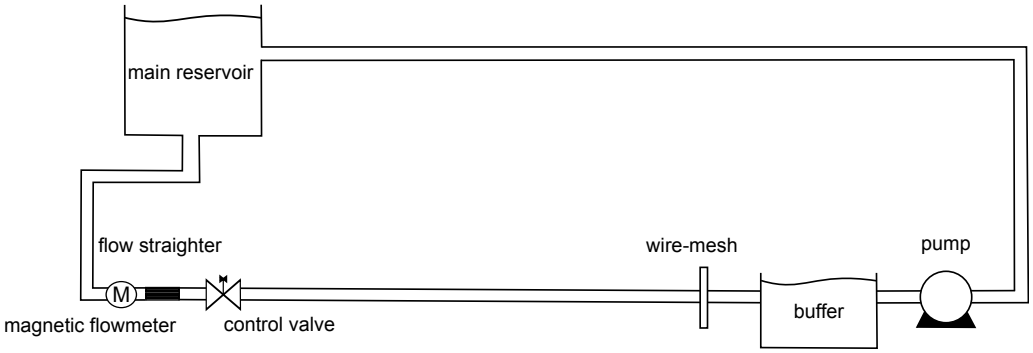

Figure 4.1: A schematic representation of the set-up

The flow is controlled by a series of valves. There are two safety valves which are capable of switching

of the flow immediately. One is electrical, the other manual. A third valve is used to set the flow to a specific flow rate. The set-up is capable of reaching velocities up to 0.5 m/s. The mean velocity of the flow is monitored by a Krohne Optiflux electromagnetic 2300 C flowmeter. In order to remove any large swirls at the beginning of the flow, the water passes a flow straightner at the beginning of the pipe.

Measurement section
At the end of the pipe there is a measurement section. Here there are several injection points and is the wire-mesh sensor installed. The used wire-mesh has 32 x 32 grid points, but since the grid is square and the wire-mesh is circular there are only 800 measurement point. The spatial resolution, i.e. the distance between the measurement points, of the wire-mesh is 3 mm. The distance between the receiver and transmitter wires is 1.5 mm; this is chosen as the probe size, as explained in section 3.1. The data is read out with a specialized data acquisition box that can be seen in figure 4.2a
In order not to disturb the flow, the injection of the tracer-fluid must be done with a capillary as thin as reasonably possible. The capillary used to inject the tracer-fluid was 1.2 mm in diameter, with an inner diameter of 0.9 mm. The tracer-fluid was injected in the center of the pipe and the capillary ran parallel with the flow direction for 13 cm. The conductivity of the tracer-fluid was 70 mS/cm and the Schmidt number was 600 (with a mass diffusivity of 2×10^{-9} m^2/s and a kinematic viscosity of 1.2×10^{-9} m^2/s. The conductivity of both the bulk-fluid in the set-up as the tracer-fluid was measured using a WTW LF340 conductivity meter.

Table 4.1: Distance to wire-mesh in hydraulic diameters ($D_h = 10$ cm), with subtraction of the capillary length.

Injection point	Distance
A	2.0 D_h
B	3.5 D_h
C	5.0 D_h
D	6.5 D_h
E	9.5 D_h

The measurement section has 5 injection points at different locations, visible in table 4.1. The tracer-fluid was injected from two 60 ml syringes simultaneously, using the Havard Instruments Phd 2000 syringe pump (figure 4.2b). The rate of injection was such that the velocity of the tracer-fluid was equal to the average velocity of the pipe. In figure 4.3 the injection of a tracer-fluid (ink) can be seen.

(a) The specialized data box. (b) The syringe pump.

Figure 4.2

4.2 Results and discussion

In the pipe flow several measurements were done. To improve the statistics ensemble measurements were performed. Because the flow is statistically stationary it is possible to average statistical properties, the spectral density or correlation functions, in order to reduce the noise. However, this only goes by $\sqrt{n}$ of the number of measurements. In table 4.2, an overview of the measurement that were done can be found. For all the measurements the tracer used was a solution of ordinary kitchen salt with a conductivity of 70.0 mS/cm, with $Sc = 600$. The measurements were done at a sampling frequency of 600 Hz. This frequency was chosen based on the spatial resolution of the wire-mesh at the highest flow rate. The distance between the receiver and transmitter wires, 1.5 mm, is considered the minimal wavelength λ_{min} that can be measured. The minimal necessary sampling frequency can be determined from both the minimal wavelength and Nyquist criterium using equation, 4.1:

$$f_{meas} = 2\frac{U_{av}}{\lambda_{min}} \tag{4.1}$$

Nyquist criterion, states that the sampling frequency needs to be a factor of two higher than the highest frequency one wants to measure. The kinematic viscosity of the water that is used to determine the Reynolds number is 1.1×10^{-6} m^2/s [31]. When the tracer is injected, it starts to move along with the

Table 4.2: Overview of the measurements done in the pipe flow set-up.

Injection point	Number of measurements	U_{av} (m/s)	Re_b	Bulk conductivity (mS/cm)	Bulk temperature (C°)
C	20	0.45	41 000	0.50-0.53	15.7-16.4
D	20	0.45	41 000	0.48-0.50	14.5-15.3
E	20	0.45	41 000	0.49-0.51	14.6-15.5
C	10	0.20	18 000	0.53-0.54	16.4-16.5
D	20	0.20	18 000	0.50-0.52	15.6-16.4
E	10	0.20	18 000	0.52-0.53	16.1-16.3

the fluid. We consider the tracer attached to fluid particles, small volumes of fluid. After injection the tracer starts to mix with the flow both by convection and diffusion. It will moving along with the fluid particles, the eddies and other structures in the flow. In the beginning the tracer will flow in a straight line, but then instabilities will form until the tracer is broken up in the smallest eddies. This can be seen by the injection of ink, as in figure 4.3 from an experiment performed by Bulk [8].

Figure 4.3: The tracer needs some development length, before it starts to follow the velocity field at the small scales. The flow goes from right to left.

Although for high enough Reynolds number the flow in the center of the pipe will show close to isotropic behavior, there always will be the effect of the wall. A good measure for the effect of the wall is the dimensionless wall coordinate y^+. For larger y^+, the effect of the wall is smaller. Using the correlations in equation 4.2 the friction factor f, the wall shear-stress τ_w, and the wall velocity u_τ can be determined.

They can be found in table 4.3. From these parameters the wall coordinate y^+ can be determined for both Reynolds numbers at any position in the pipe.

$$\begin{aligned} 4f &= 0.316Re^{-\frac{1}{4}} \\ \tau_w &= \frac{\rho U_{av}^2 f}{2} \\ u_\tau &= \sqrt{\frac{\tau_w}{\rho}} \\ y^+ &= \frac{u_\tau y}{\nu} \end{aligned} \tag{4.2}$$

Table 4.3: Flow properties for the pipe flow.

Re	f	τ_w (Pa)	u_τ (m/s)
18 000	6.8×10^{-3}	0.136	1.2×10^{-2}
41 000	5.6×10^{-3}	0.56	2.4×10^{-2}

Scalar spectral density
In figure 4.4, the scalar spectral density $\phi_s(\kappa)$ and the pre-multiplied spectra are plotted for both Reynolds numbers for the injection points C, D and E. The spectra are calculated at pixel $(14, 17)$, where $r/R = 0.15$. This is equal to $y^+ = 451$ for $Re = 18\ 000$ and $y^+ = 916$ for $Re = 41\ 000$. The pre-multiplied spectrum is made by multiplying the values $\phi_s(\kappa)$ from the normal spectral density with their corresponding κR values. The pre-multiplied spectrum is an alternative way of plotting the spectral density and has as an advantage that equal areas under the curve correspond to equal energies. It also magnifies the center part of the curve, such that variations in the spectrum are better visible.

The spectral densities are normalized such that the area under the curve is equal to the mean-square of the scalar fluctuation, as in equation 4.3. This normalization is according to Hinze [32].

$$c'^2 = \int_0^\infty \phi_s(\kappa) d\kappa \tag{4.3}$$

The injected fluid is more dispersed when measuring further from the injection point. As a result, c'^2 will decay when going from injection point A to E. Because the wire-mesh sensor is not calibrated such that the output is translated in an actual concentration of salt, c'^2 is not the real fluctuation in concentration, but the mean-squared fluctuation in the signal. Since these fluctuations in the signal and in the concentration scale linearly and the same conductivity of tracer-fluid is used for every measurement, the spectra scale relatively to each other in the right manner.

After injection, the tracer-fluid needs some development length before the spectral density gets its definitive shape. By examining the pre-multiplied spectra, it can be seen that primarily at the lower dimensionless wave-numbers, around $\kappa R = 3$, the shape of the spectrum changes when moving from injection point C to E. Because the change in the shape of the spectrum is marginal between point D and E, we will consider the spectral density of point E as fully developed. The data of this point will be used when further evaluating the results of both the measurements in the pipe flow and in the rod-bundle axial flow.

The set-up did not have any injection point further upstream than point E to check whether the spectrum is really fully developed. If in future research injection points further away from the measurement section are used, the properties of the tracer have to be taken into account. The density difference of the tracer-fluid with the water was such that, especially for lower Reynolds numbers, buoyancy effects start to play a role at larger distances, as already observed by Bulk [8].

Taking a closer look to both normal spectral densities in figure 4.4a and 4.4c there are several noteworthy

things. For the $Re = 41\ 000$ flow the spectrum is constant up to $\kappa R = 3$. From that point, it decreases with a κ^{-1} dependency to $\kappa R = 50$. After this, the spectrum gets a much steeper slope. The spectrum of the $Re = 18\ 000$ shows a similar kind, but slightly different behavior. It is constant up to $\kappa R = 2$, from which it starts to decrease. The curve is a little less steep than the κ^{-1} curve in the $Re = 41\ 000$ flow and bends to a steep line at $\kappa R = 50$.

A κ^{-1} dependency will show up in the pre-multiplied spectrum as a horizontal line. In figure 4.4b this is clearly visible and shows that the spectrum have a very precise κ^{-1} dependency. The pre-multiplied spectrum of the $Re = 18\ 000$ flow in figure 4.4d shows shows a a slightly increasing curve from $\kappa R = 2$, meaning that indeed this spectrum follows a κ^{-p} curve with $p \approx 0.8$. There is a blunt peak in the spectrum at $\kappa R = 20$, corresponding to a wavelength of 1.5 cm which could be a dominant structure size in the flow. However the bump, is in the part where the normal spectrum start to decrease rapidly. The reason for the decrease is that approaches the spatial frequency of the wire-mesh sensor. As a consequence, it is not possible to say how the curve continuous from the maximum, based on this measurements.

The abundance of a $\kappa^{-\frac{5}{3}}$ dependency in the spectral density is noteworthy. Such a dependency would mark the inertial subrange in the eddy cascade model. This means that the pipe flow does not satisfy isotropic turbulence at the Reynolds numbers of the measurements. Since the model assumes unbounded flow at very high Reynolds number, this was to be expected.

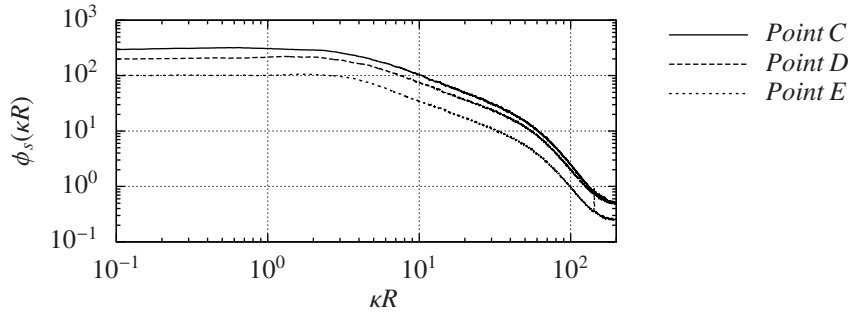

(a) The scalar spectrum of ensemble measurements at $Re = 41\ 000$ for injection point C, D and E.

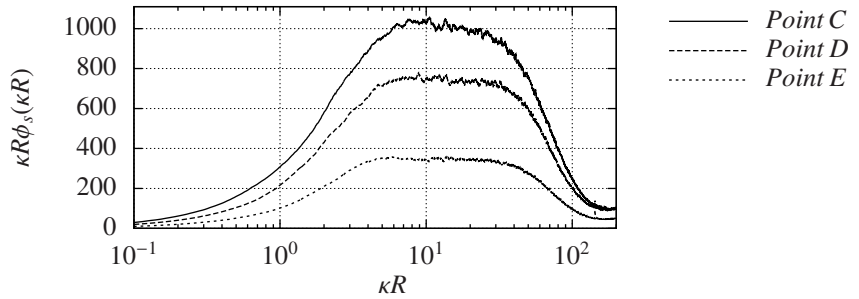

(b) The pre-multiplied scalar spectrum of the measurements in figure 4.4a.

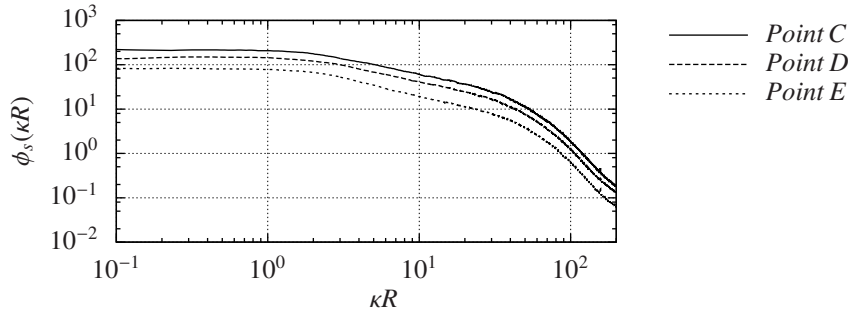

(c) The scalar spectrum of ensemble measurements at $Re = 18\ 000$ for injection point C, D and E.

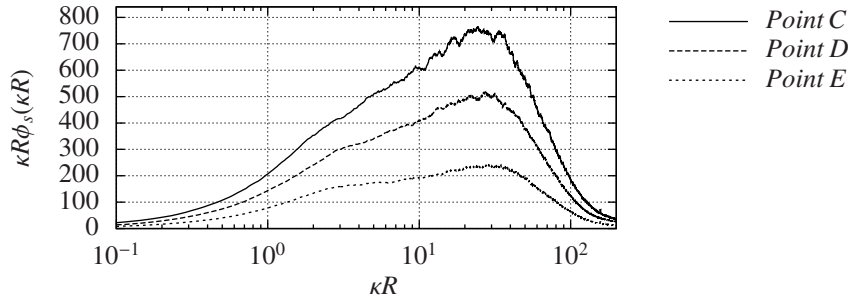

(d) The pre-multiplied scalar spectrum of the measurements in figure 4.4c.

Figure 4.4: The scalar- and pre-multiplied scalar spectrum of the measurements in the pipe flow at $Re = 41\ 000$ and $Re = 18\ 000$ at $r/R = 0.15$. The spectral densities are normalized with the mean squared signal fluctuations.

Comparison with literature

In order to verify the results for the power spectral density, an experimental study of Nye and Brodkey [33] was chosen. They did measurements of the scalar spectrum in a pipe flow with a diameter of 7.8 *cm* and a centerline Reynolds number of 50 000. This Reynolds number close is enough to the Reynolds number of 41 000 used in this research, in order to compare. The passive scalar they measured was 'concentration of blue ink' with $Sc \approx 4000$. Their measurement technique consisted of measuring the transmission of light through translucent sections of the pipe with a fiberglass probe. The measurement points were at 4, 24 and 36 pipe diameters downstream from the injection point.

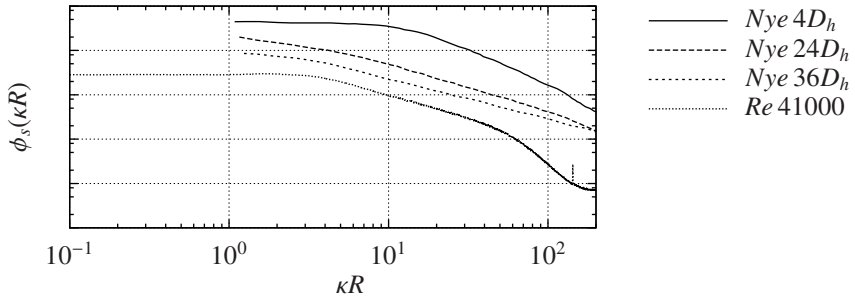

(a) The spectral densities of the measurements in figure 4.4 at point E and the measurements of Nye and Brodkey.

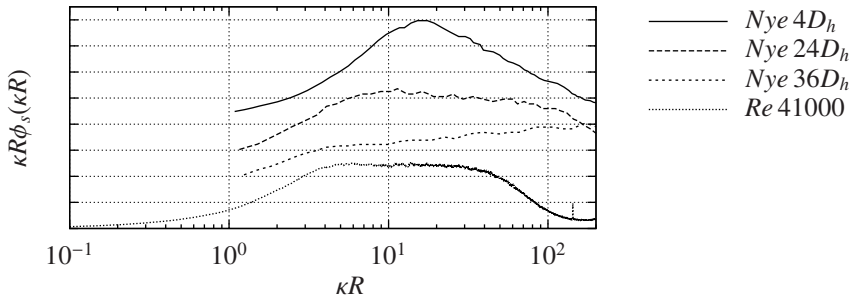

(b) The pre-multiplied scalar spectra of figure 4.5a.

Figure 4.5: Scalar spectra of a pipe flow for the measurements of Nye and Brodkey at $Re = 50.000$ at the center of the pipe and with $Re = 41\ 000$ at $r/R = 0,15$ for the measurement at point E of the current research. The spectra are plotted with an offset with respect to each other.

In figure 4.5 both the results of Nye and Brodkey and the results of the current research with $Re = 41\ 000$ at injection point E are plotted. The results of Nye show a clear κ^{-1} behavior for the 24 D_h and 36 D_h injection points. Because the results of Nye and Brodkey are calibrated to actual concentration, it was decided to just plot the spectra with an offset with respect to each other. For comparing the scalar spectra, we consider the shape of the spectrum is more important than the units at the y-axis.

In figure 4.5, the development of the spectrum from the measurements of Nye and Brodkey can be observed. The spectrum of the measurement at 4 pipe diameters has a lot of energy in the small wave-numbers and this energy moves to higher wave-numbers for measurements further downstream. This is the result of the mixing of the tracer, when following the structures, eddies and swirls in the flow.
The measurement of Nye at 24 pipe diameters seems to match the measurement of the $Re = 41\ 000$ flow. Both have a κ^{-1} dependency in the same interval of wave-numbers. The measurement of Nye at 36 diameters seems to have a dependency of κ^{-p} with $p < 1$, but this is only the case for the higher wave-numbers. The deviation from the κ^{-1} curve is probably because of applying a correction factor to compensate for the fact that the probe of the sensor is of finite size. More on this correction factor can be found on the next page.

The measurements of Nye and Brodkey lack the presence of a $\kappa^{-\frac{5}{3}}$ dependency too. To explain the lack of a $-\frac{5}{3}$ curve and and the existence of a κ^{-1} curve they came up with a theory on the mixing process of

the tracer-fluid. It is based on the theory as proposed by Bachelor [16] for the presence of a κ^{-1} in passive scalar measurement at scales smaller than the Kolmogorov length-scale. Bachelor predicts a -1 curve for wave-numbers larger than the the Kolmogorov wave-number by arguing that at the Kolmogorov scale the break-up of eddies stops. The passive scalar is not limited by this scale and can be measured at smaller length-scales. At this scale the tracer is transferred to smaller scales by the deformation of fluid particles due to stretching and straining. The theory of Nye and Brodkey is that for the Reynolds number of the current measurements the scalar is transferred to smaller length-scales by the same mechanism, which causes the κ^{-1} dependency.

Correction factor

In figure 4.5a, a bent in the spectrum of $Re = 41\ 000$ and $Re = 18\ 000$ around dimensionless wave-number $\kappa R = 50$ can be observed. Because the 'probes' of the the wire-mesh sensor are of finite size, not all wavelengths can be measured. Wavelengths smaller than the probe size cannot be determined, however, they can be detected. This gives an error in the results, which can be corrected for. The error starts approximately from the point where the κ^{-1} curve becomes steeper. Nye and Brodkey used a correction factor developed by Uberoi and Kovasznay [34], which was originally developed for hot-wire anemometry. Their correction model multiplies the entire spectrum with a correction factor. The factor is 1 for small wave-number and increases rapidly for the large wave-numbers. Attempts to apply this correction factor on the current measurements were not successful. This is not problematic, because this research focuses on large-scale coherent structures, but for using the wire-mesh in experiments were wavelengths close to the probe size are of interest, a correction method has to be constructed.

Dispersion

In figure 4.6a the mean concentration at different distances from the injection point in the radial direction is plotted. Again, since the wire-mesh is not calibrated to an actual concentration, 'signal units' are used. The concentration in the radial direction follows a Gaussian distribution, which can be explained by the random walk behavior in the radial direction, according to Taylor's theory of turbulent dispersion for large time-scales. The tracer displacement along the centerline in the radial direction satisfies equation 2.9, creating a parabolic plume of tracer-fluid.

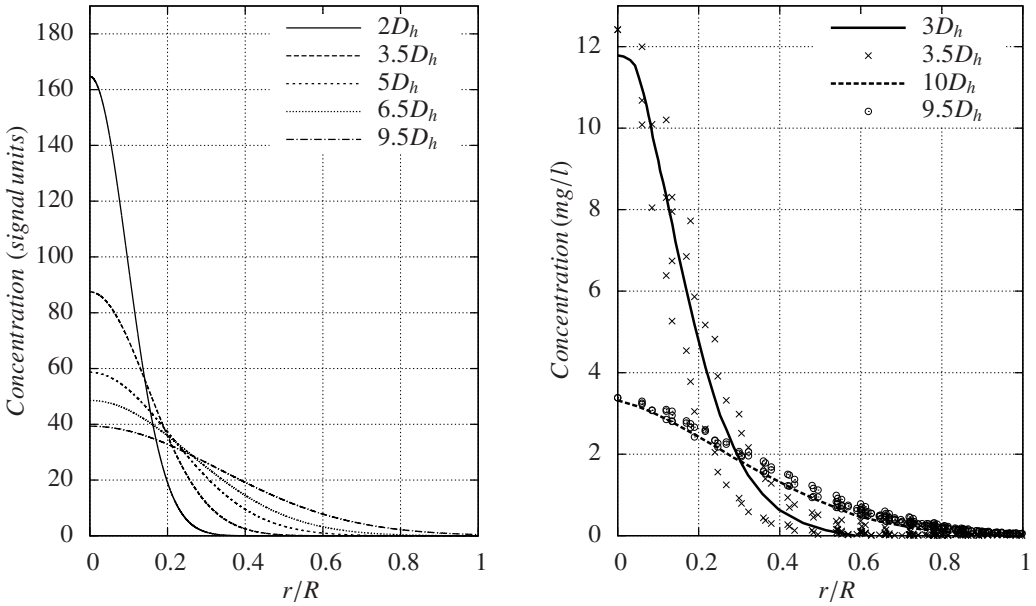

(a) Dispersion at $Re = 41\ 000$.

(b) Comparison of the wire-mesh sensor results, crosses and circles, with measurements from Lee and Brodkey [35], line and dashed line.

Figure 4.6: The dispersion as measured with the wire-mesh and compared with the measurements by Lee and Brodkey [35] using ink and a light-probe.

In figure 4.6b the dispersion measurements are compared with the the measurements of Lee and Brodkey, for two different injection points. Because their results are calibrated to a concentration, the results of the wire-mesh sensor are multiplied with a scalar, such that the curves overlap. Since the dispersion is independent of the concentration this is valid.
The measurements of 9.5 and 10 pipe diameters overlap very good. The measurement of 3 and 3.5 pipe diameters overlap qualitatively too, but the measurement with the wire-mesh sensor suffers from large variance. This is because of reasons described in calibration section 3.3.1. The wire-mesh is not very good in measuring concentrations, since different pixels give different responses, particularly for large concentration differences.

Probability density function
Just like the velocity, a passive scalar can be decomposed into a mean and a fluctuating component, $C = \overline{C} + c'$, in which it is assumed that the behavior of c' will be similar to that of u'. The behavior of the fluctuating part of the concentration, c', can be quantified by constructing a probability density function of the fluctuation. This is done by computing the probability of a certain change in the fluctuation in a certain time domain. We will call this change $\Delta c'(t)$ and it is defined as in equation 4.4:

$$\Delta c'(t) = c'(\tau) - c'(\tau - t) \tag{4.4}$$

So $\Delta c'(t)$ is the difference between the values of the fluctuating part of the concentration c', over a fixed time t. By computing this difference at any point of a time-series, the pdf of $\Delta c'(t)$ can be determined. This pdf can be a manner to study, for example, the effect of different eddy-sizes (using Taylor's hypothesis to translate time into space) on c'. In this research, just a qualitative analysis is done, since this is a highly specialized field in turbulence. The goal of this part of the research is just to demonstrate that the wire-mesh sensor is capable of making such measurements.

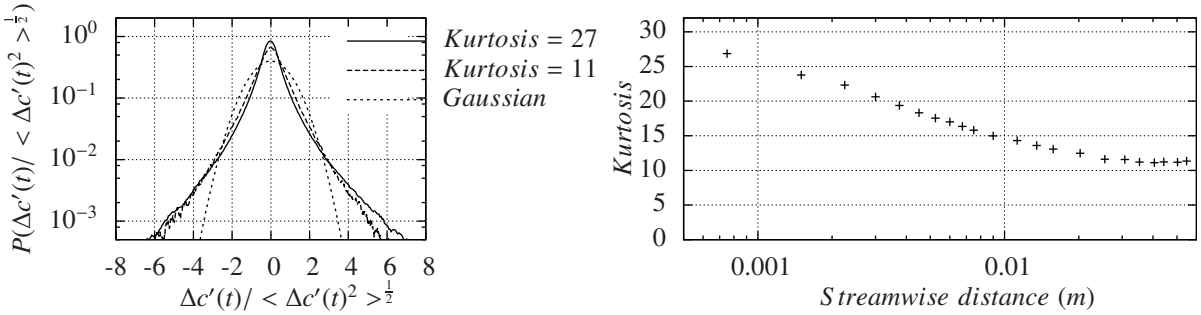

(a) The normalized pdf at different Δt in $\Delta c'(t)$ compared with a gaussian distribution.

(b) The kurtosis of different Δr in c'.

Figure 4.7: The pdf and kurtosis of different Δr in c' normalized with respect to it's root-mean-square at r/R=0.15. Δr was determined from the time-series using Taylor's hypothesis.

In figure 4.7a the pdf of $\Delta c'(t)$ over the smallest possible time-step of the measurement at $Re = 41\ 000$ can be seen together with the pdf to which the distribution of the fluctuations converge over larger times (hence distance) in the same measurement. These curves correspond to the first and the last crosses in figure 4.7b. As a reference, also a normal distribution is plotted. Figure 4.7b shows the kurtosis of the pdf of $\Delta c'(t)$ at different distances. It can be observed that the kurtosis is large at small length-scales and converges to a value of 11 for larger length-scales in about 3 to 4 cm. Comparing these results with the DNS results of Chen and Kraichnan [36] in figure 4.8 the following can be noticed.

Chen and Kraichnan simulated a two-dimensional nominally isotropic random advection by a white velocity field in an unbounded flow. In their results the kurtosis is large for small scales and then converges to 3 for large length scales in approximately 40 cm . This means that distribution of the fluctuations in c' for large r converge to a Gaussian distribution. The shift from large kurtosis for small scales to small kurtosis for large scales is qualitatively is similar to the pipe flow. However, the pdf in the pipe flow did not converge to a normal Gaussian distribution. The difference can be explained by

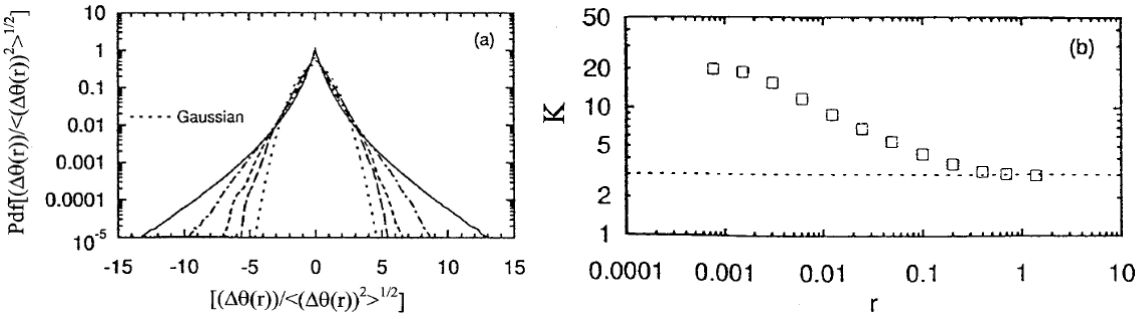

Figure 4.8: The pdf and kurtosis for scalar fluctuations, simulated via DNS by Chen and Kraichnan [36].

the fact that the simulation was done for a completely different flow. Namely two dimensional isotropic unbounded flow, against the three dimensional bounded flow that is not really isotropic.

One-point correlation

The auto-correlation is a measure of causality in a signal with itself. In other words, does the signal depends on previous values, or is it random. It is defined as a convolution of the time-series with itself as in equation 4.5:

$$R_{xx} = \frac{1}{T}\int_0^T x(t) \cdot x(t+\tau) d\tau \tag{4.5}$$

It is common to normalize the auto-correlation such that the correlation at $t = 0$ is 1. In figure 4.9 the normalized auto-correlation functions of the measurements of both Reynolds numbers at 9.5 D_h are plotted. Again, the time is converted to a distance using the average velocity.

A higher correlation means a stronger causal relation with previous values. For both Reynolds numbers the correlation drops to 0 at 7 cm. This means that after 7 cm there is no longer a causal connection in the signal, which is also a measure for the typical structure size in the flow. The correlation function for $Re = 18\ 000$ is always positive, but the correlation at $Re = 41\ 000$ becomes negative at 3 cm. A negative correlation is typical for the presence of more complex structures in the flow, such as counter rotating swirls. From the correlation function in time, the Taylor micro-scale λ, defined in equation 4.6a, can be determined together using the Taylor's hypothesis as in equation 4.6b. The Taylor microscale is often used as a measure for the eddy size in the intermediate scales.

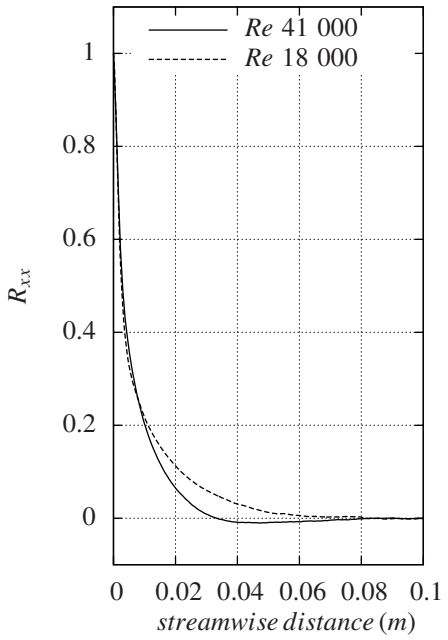

Figure 4.9: The auto-correlation of both Reynolds numbers, at r/R = 0.15.

$$\frac{1}{\lambda^2} = -\left.\frac{\partial^2 R_{xx}}{\partial r^2}\right|_{r=0} \tag{4.6a}$$

$$\frac{\partial^2 R_{xx}}{\partial r^2} = \frac{1}{\overline{u'^2}}\frac{\partial^2 R_{tt}}{\partial t^2} \tag{4.6b}$$

The variable $\overline{u'}$ can be approximated by u_τ. The Taylor microscale is determined to be 8×10^{-5} m for both Reynolds numbers. Since the Taylor microscale scales with $Re^{-\frac{1}{2}}$ (Tennekes and Lumney [37]) this is not a very reliable result. This is probably due to the fact that the spatial resolution of the wire-mesh sensor is too low for such small length-scales. However, a Taylor microscale in time could be determined in a similar manner, using equation 4.7:

$$\frac{1}{\lambda^2} = -\left.\frac{\partial^2 R_{xx}}{\partial t^2}\right|_{t=0} \tag{4.7}$$

This gives a Taylor microscale of $\lambda = 6.5 \times 10^{-3}$ s for the $Re = 41\ 000$ flow and of $\lambda = 3.4 \times 10^{-3}$ for the $Re = 18\ 000$ flow. These results are just above the time-resolution of 600 Hz. The physical meaning of the Taylor micro-time-scale is quite complicated, since it is not really a time-scale. The Taylor microscale is usually interpreted as a length-scale for the intermediate scale, so the Taylor micro-time-scale could perhaps be interpreted analogously as a time-scale for the intermediate scale.

Multi-point correlation

A nice feature of the wire-mesh is that is has probes in the entire cross section of a flow. Because of the multiple probes in the wire-mesh sensor, besides constructing the correlation function of the time-series of one pixel with itself, it is also possible to construct the correlation function of one pixel with all other pixels. The correlation function between the time-series of two different pixels is called the cross-correlation. It is defined as the convolution between the two time-series as in equation 4.8:

$$R_{xy} = \frac{1}{T} \int_0^T x(t) \cdot y(t+\tau) d\tau \tag{4.8}$$

This way the correlation of a certain point with the flow around it can be obtained for different time-lags. Using Taylor's hypothesis, the time-lag is converted to a distance, creating a correlation function of certain point with the space around it. The cross-correlation is normalized, similar to the auto-correlation, such that the cross-correlation at $t = 0$ of pixel x with itself is 1. In figure 4.10 the two-dimensional cross-correlation function of a the same pixel used in figure 4.9 is plotted at $r/R = 0.15$ for both Reynolds numbers. It shows the correlation function along the diameter of the pipe in the y-axis and along the streamwise direction of the pipe in the x-axis.

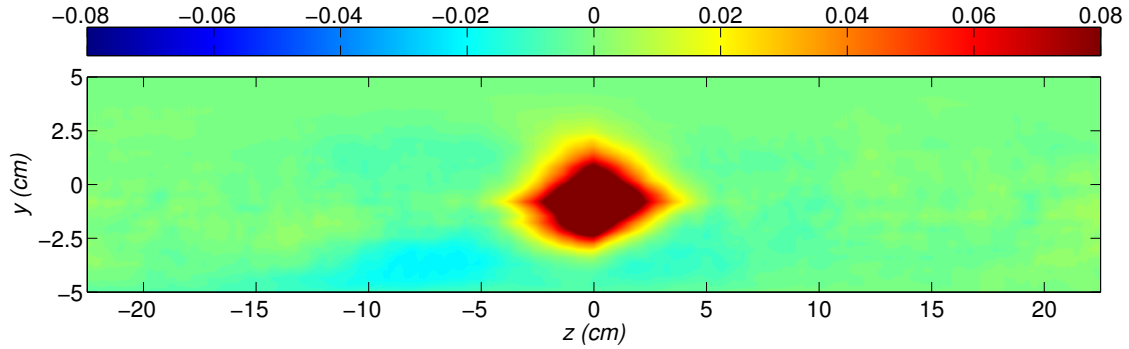

(a) $Re = 18\ 000$

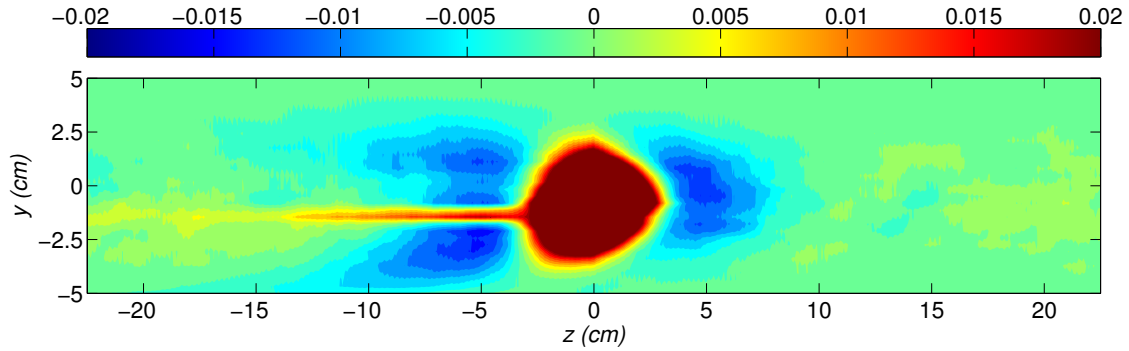

(b) $Re = 41\ 000$

Figure 4.10: Multi-point cross-correlations of a point along the diameter of the pipe and along the streamwise direction.

As mentioned before, the correlation function is a measure for the eddy-size in the flow. The multi-point cross correlation makes is possible to determine the shape of the eddies too. The two-dimensional way

of plotting with a color gradient makes it difficult to determine the exact size of the eddies, because the 'color-resolution' gives a deceiving effect. The correlation drops very fast over a short range, so the correlation coefficients of larger structures are relatively small and become invisible. To solve for this, the color range is adjusted to make these correlations appear.
Both figure 4.10a and 4.10b show an elongated eddy-structure. Since the eddy is confined by the wall and not in the streamwise direction, this was to be expected. The cross-correlation function of the $Re = 18\ 000$ flow drops to 0 in a couple of centimeters, as was already concluded with the auto-correlation. The $Re = 41\ 000$ flow has an area of a slightly negative correlations, reaffirming the existence of counter-rotating structures.
The long tail in figure 4.10b is due to some pollution, or dirt, in the wire-mesh sensor.

4.3 Conclusions on the pipe flow

Based on the measurements with the wire-mesh sensor in the pipe flow several conclusions can be made. These conclusions are a quick summary of the results, a more extensive discussion can be found in chapter 6.

On passive-scalar measurement using a wire-mesh sensor

- *Ensemble averaging is a suitable method to reduce the variance in the calculation of statistical flow properties like correlation functions and spectral densities.*: Because the reduction follows $\sqrt{N}$ behavior with the number of measurements, this method is practical for 10 to 20 data sets.
- *The Welch Overlapped Segment Averaging (WOSA) method is a good method to determine the power spectral density of the passive-scalar measurements with the wire-mesh sensor*: The method combines relative short computation times with significant variance reduction.
- *A wire-mesh sensor can be used to construct the probability spectral density of the fluctuations of a passive scalar*: Here too, the wire-mesh sensor has the advantage over other measurement techniques, since it is able to do measurements in an entire cross-section of the flow, hence to determine the PDF of the passive-scalar fluctuations simultaneously in the whole cross-section of the flow.
- *Passive-scalar measurement can be done with a wire-mesh sensor with a spatial resolution in the order of millimeters and with a time resolution up to* 1 kHz: The spatial resolution is limited by the distance between the transmitting and receiving wires, which makes the wire-mesh sensor suitable for studying the large scale structures in a flow. Measurements in the order of minutes are needed in order to determine the statistical properties of the flow. These long measurements are, with the current software, limited to a frequency of 1 kHz.

On passive-scalar measurements in pipe flow at Reynolds numbers 18 000 and 41 000

- *The scalar spectral density in pipe flow at* $Re = 41\ 000$ *shows a* κ^{-1} *dependency*: This is measured in this research and is consistent with the work of Nye and Brodkey [33].
- *The scalar spectral densities of the* $Re = 18\ 000$ *flow shows a* $\kappa^{-0.8}$ *decay*: This is a slightly different spectrum than the spectrum of the $Re = 41\ 000$ flow. No literature was found for passive-scalar measurements in the core of a pipe flow at $Re \approx 20\ 000$, so no verification can be done.
- *Pipe flow at intermediate Reynolds numbers produce elongated structures in the order of the pipe diameter*: This follows from the auto-correlation- and cross-correlation functions. The elongated shape was to be expected since the wall forms a physical boundary for structures and confines their growth.
- *Concentration fluctuations in pipe flow do not converge to a normal distribution*: This is different from isotropic turbulence, so the flow in the center of the pipe cannot approximated as such.

Chapter 5

Rod-bundle axial flow

In this chapter the results of the measurements in a rod-bundle geometry are discussed. Here, the advantages of the wire-mesh sensor become clear. The complex geometry of the rod-bundle makes it very hard to use techniques which require optical access, such as PIV. Van Campen [6] made an attempt using refractive index-matching, but this remains a complicated procedure. The wire-mesh sensor is relatively easy to implement in the set-up and when using a passive scalar not only the flow statistics can be measured, but it is also possible to create images of the flow structures. The results in this chapter are a next step in using the wire-mesh sensor for finding coherent structures in a rod-bundle geometry and determining their dependency on the flow velocity.

5.1 Coherent structures

Every flow has a velocity field which determines the movement of the fluid particles. The velocity field can contain a certain degree of order. This order, although a somewhat vague concept, is the broadest definition of a coherent structure in a flow. As already discussed in section 2.1, the most common structure in turbulent flows is the eddy. However, coherent structures do not exist solely in turbulent flows, they can be formed in laminar flows as well. Well known coherent structures in fluid dynamics are the Von Karman vortex street and Kelvin-Helmholtz instabilities. It needs to be stated explicitly that, although these structures are swirling motions, the mechanism that forms them is not turbulence. The Von Karman vortex street, for example, is created by the vortices that form in the wake behind a cylinder. From Reynolds numbers higher than about 50, these vortices start to oscillate in an unstable manner, which causes them to break loose from the wake one at the time. The vortices that break free are very stable and long living, creating a street of vortices as in figure 5.1.

Kelvin-Helmholtz instabilities
It is assumed that inside a rod-bundle geometry there also exist coherent vortices. The mechanism that forms these structures would be the shear-stresses between different regions in the flow due to velocity or density differences. Shear-stresses between layers of a fluid are known to cause coherent structures, these are called Kelvin-Helmholtz (K-H) instabilities. In figure 5.2 an example of Kelvin-Helmholtz in daily life can be seen. The existence of Kelvin-Helmholtz instabilities can be derived by hand and can be found in appendix B. The derivation consists of a stability analysis of a perturbation on the interface of two layers of fluid with different uniform velocity and density. The solution consists of a set of modes that are stable or unstable, depending on the velocity- and density differences in the fluid layers. When there is no density difference, as in the rod-bundle, all modes are unstable and perturbations will always grow.

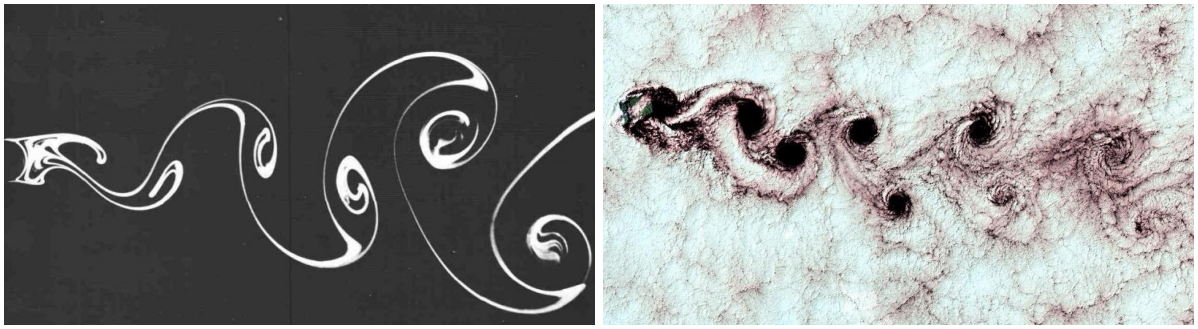

Figure 5.1: An examble of coherent structures: The Von Karman vortex sheet consists of several long living vortices and can be formed both at small scales in a laboratory (left, from Van Dyke [38]) and at large scales, around islands (right).

Figure 5.2: An example of Kelvin-Helmholtz instabilities in the environment.

Structures in the rod-bundle geometry

As mentioned before, it is very important for the stability and safety of a nuclear reactor, to have a good understanding of the transport and mixing of heat by water inside the reactor vessel. Coherent structures could be a major contributing factor in the mixing rates, so it is important to have good understanding of their existence and their properties. From the paper of Rehme [4] it becomes clear that, after years of research, there still is a controversy about the existence of coherent structures in rod-bundles. If they exist, they probably form because of the shear-stresses in the fluid, just like Kelvin-Helmholtz instabilities. Recalling the internal structure of a rod-bundle in figure 5.3, the rod-bundle has roughly two different parts were the water can flow through; the subchannel and the gap. The subchannel is much wider than the gap, with a large difference in friction. This can cause a large gradient in the velocity between the gap and the subchannel, resulting in a large shear-stress at the interface between the two areas. A situation that might be similar to the circumstances in which Kelvin-Helmholtz instabilities form and what can lead to the formation of large-scale coherent-vortices. The pitch to diameter ratio, defined as the ratio between the distance between the centers of two rods, the pitch P, and the diameter D of the rods, plays an important role here. If the gap is too small, all instabilities will be damped out by

friction, if the gap is to wide, there is no large velocity-gradient between the gap and the main channel, hence no shear-stresses. When the rods are too big, the subchannel will become very small and friction will damp all instabilities, when the rods are too small, the gap becomes too wide and there will be no large velocity-gradient. The controversy in this problem is whether there exists, or not, a range of pitch to diameter ratios where the circumstances are just right for the formation of coherent structures.

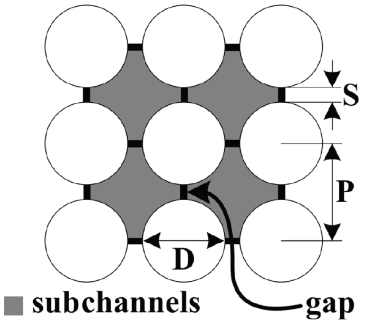

Figure 5.3: Large coherent-structures might form if the pitch to diameter ratio is just right, from Bulk [8].

5.2 Set-up

The rod-bundle geometry used in the experiments is a vertical gravity-driven axial flow with 2x2 rods, used before by Van Campen [6] for LDA measurements and later by Bulk [8] for passive-scalar measurement with a wire-mesh sensor. It was built from 6 rectangular PVC sections of 1 m each. Inside 4 PVC rods with a diameter of 25 mm were placed and kept from the wall with specially designed spacers, which minimize the disturbance of the flow. On the sides of the sections parts of rods were glued, in order to simulate a bigger geometry and effectively creating 9 subchannels as visible in figure 5.4.

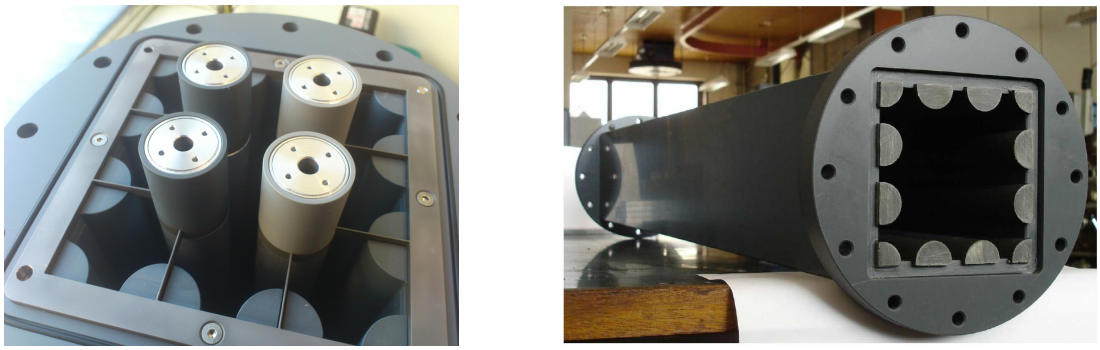

Figure 5.4: A section from the rod-bundle set-up, with a close-up of the rods, from Van Campen [6].

Schematic overview of the set-up

The rod-bundle is built similar to the pipe flow, as can be seen in figure 5.5. The flow through the rod-bundle is gravity driven in order to prevent from pulsations by a pump. Just like the pipe flow, the rod-bundle has two water reservoirs, one at the top and one at the bottom. After the water flows from the top reservoir through the rod-bundle, the water is pumped back up. An overflow vessel keeps the rod-bundle at constant pressure and the flow rate is controlled by a set of rotameters. To minimize any disturbance a flow straightner is installed at the entrance of the rod-bundle and the flow has a development length of approximately 135 D_h before the wire-mesh sensor, and 25 D_h after the sensor. The maximum Reynolds number that could be achieved with the set-up was $Re = 6000$.

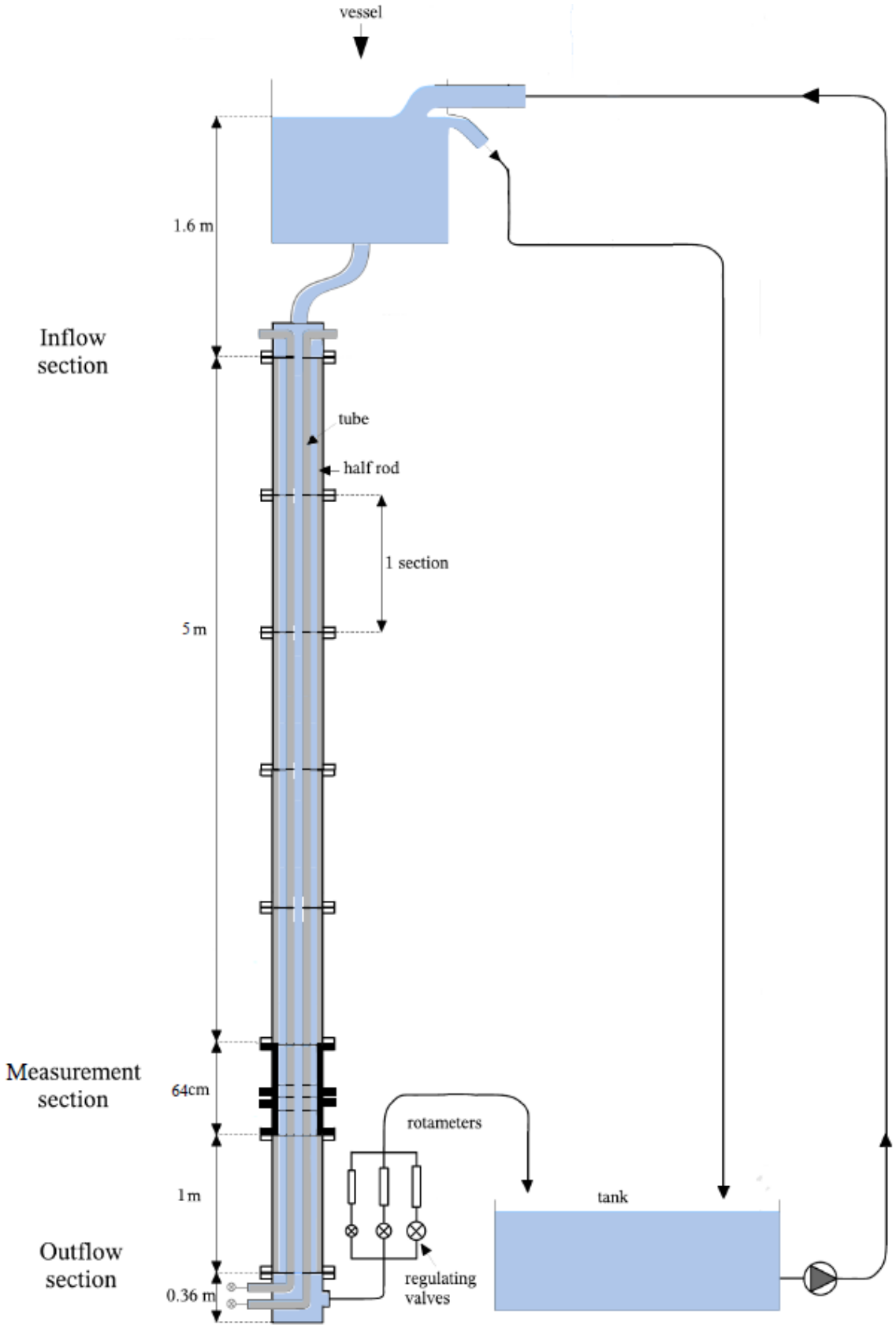

Figure 5.5: A schematic representation of the vertical rod-bundle axial flow set-up, from Bulk [8].

Detailed description of the cross-section

The parameter that affects the formation of coherent structures is the pitch to diameter ratio P/D. The choice for this ratio is based on the work of Ikeno and Kajishima [39], in order to be able to compare the experimental results with their numerical simulations. These results indicated a P/D ratio of 1.4 as a good candidate. With the diameter and the P/D ratio fixed the resulting cross section of the flow looks like figure 5.6.
In order to determine the hydraulic diameter D_h equation 5.1 is used. In this formula A is the surface of the cross-section of the flow and Q is the wetted perimeter.

$$D_h = \frac{4A}{Q} \tag{5.1}$$

From the dimensions of figure 5.6 the hydrolic diameter of one subchannel is determined to be $D_h = 4\ cm$.

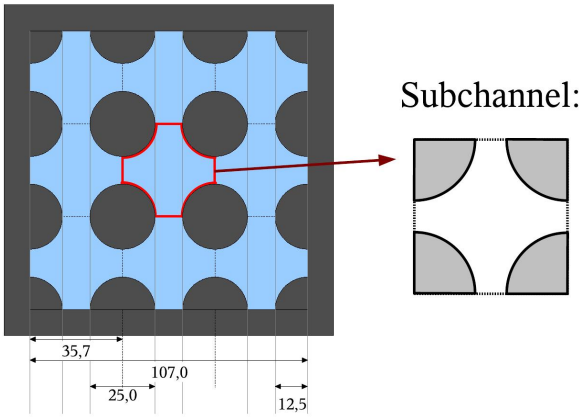

Figure 5.6: A detailed view of the cross-section of the flow, dimensions in mm. The close-up of the subchannel is used to determine the hydraulic diameter which is $D_h = 4\ cm$.

Measurement section

The dimensions in the developing part of the set-up deviate a little from the dimensions in figure 5.6, due to the construction method with a lot of parts. Besides, the material properties of the PVC cause the rods to be flexible. To get more reliable measurements a special measurement section was constructed. This special part of the rod-bundle reaches from 12.5 D_h above the wire-meshes to 2.5 D_h below the wire-meshes. The higher accuracy is achieved by milling the outer part of the the rod-bundle in one piece and by using aluminiums rod to prevent flexing.

Instead of one, two wire-mesh sensors, with 32 x 32 grid points each, were installed in the rod-bundle. The advantage of an extra wire-mesh is that it gives the possibility to measure the tracer-fluid in the streamwise direction. The two sensors are placed one hydraulic diameter apart. Because the data acquisition box is only capable of dealing with 32 x 32 grid points, only the center pixels were used. This gives an effective wire-mesh of 32 x 16 grid points. Because the set-up is symmetric in the xy-plane, this is not a problem. The distance between the transmitting and the receiving wires was 1.5 mm and the thickness of the wires was 0.2 mm. This is thin enough in order to minimize the disturbance in the flow.

In order to cope with the rods passing the wire-meshes, special PVC connectors were constructed. These connectors guide the rods through wire-mesh sensors, while insulating the wires from the aluminium rods, so that the electric signal is not disturbed. They and can be seen in figure 5.7.

The injections points on the rod-bundle set-up are at 1, 4, 7 and 10 D_h upstream of the first wire-mesh sensor. For this research only the 10 D_h injection point was used, based on the experience of the pipe flow experiment. Also, for the results presented in this chapter the tracer-fluid was injected above the middle of the gap. The capillary used to inject the tracer-fluid was of the same dimensions as that of the capillary used in the pipe flow experiment, so an outer diameter of 1.2 mm and a inner diameter of 0.9 mm. The tracer-fluid was identical as well; a kitchen salt solution with a conductivity of 70.0 mS/cm and a Schmidt number of $Sc = 600$.

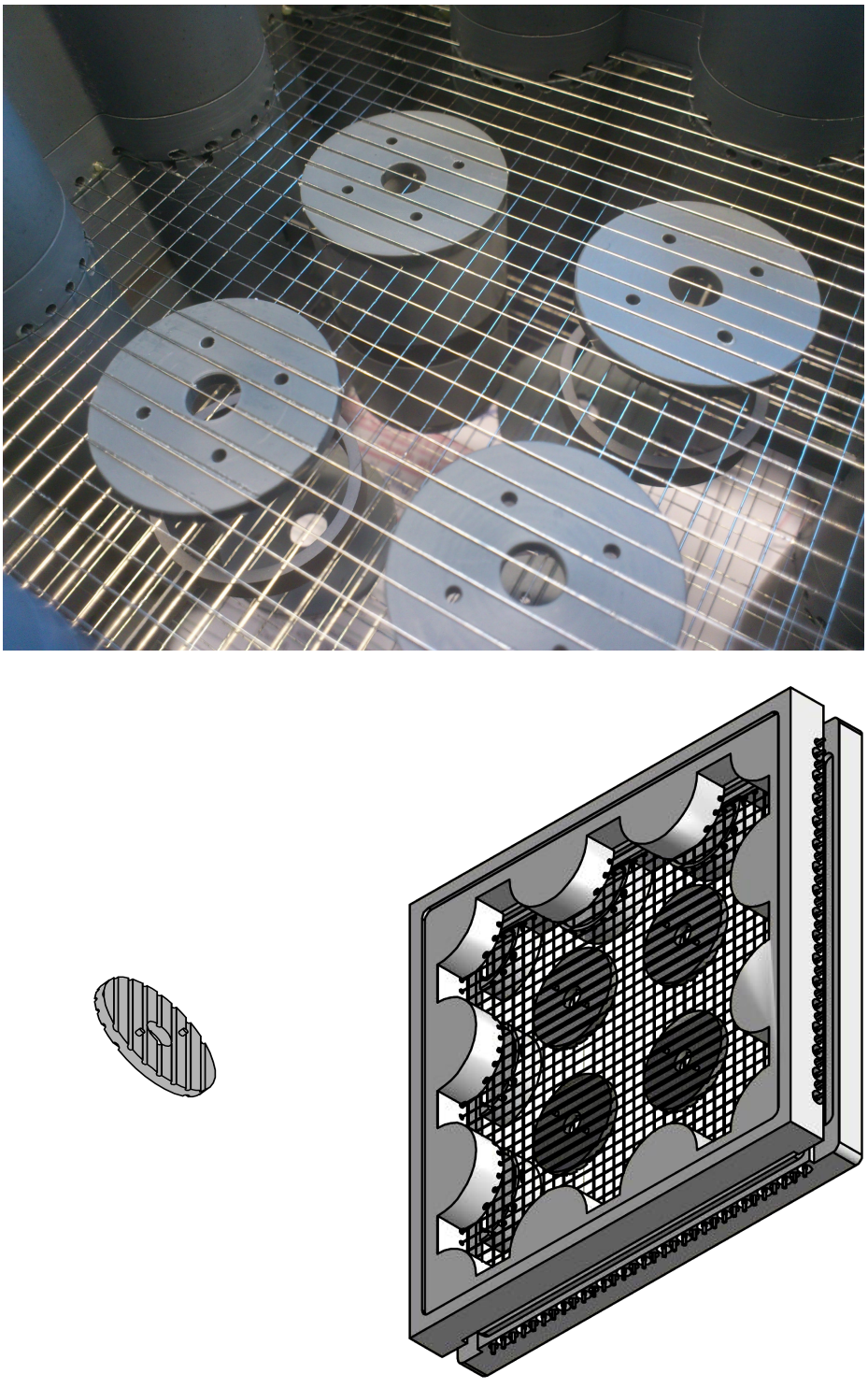

Figure 5.7: The wire-mesh in the rod-bundle needs special spacers to guide the rods through the sensor without disturbing the signal, from Bulk [8].

5.3 Results and discussion

In the rod-bundle geometry a sweep across the full range of Reynolds numbers in the set-up was measured. All results are composed of an ensemble set of 14 measurements an overview of all measurement series is given in table 5.1. The measurements were done at a frequency of 500 Hz, the properties of both the tracer-fluid and the water was the same as in the pipe flow experiment. If the subchannel is assumed to be like a pipe flow, the wall shear-stress and the wall velocity can be estimated for the turbulent flows, using the hydraulic diameter and the equations 4.2. For the laminar flow the friction factor in equation 5.2 has to be used:

$$4f = \frac{64}{Re} \tag{5.2}$$

Although these equations actually are for a pipe flow, they can give a crude estimate for the properties of the rod-bundle axial flow. Since the flows of $Re = 1500$ and $Re = 3000$ are around the transition regime between a laminar and a turbulent flow, the approximation is even more poor.

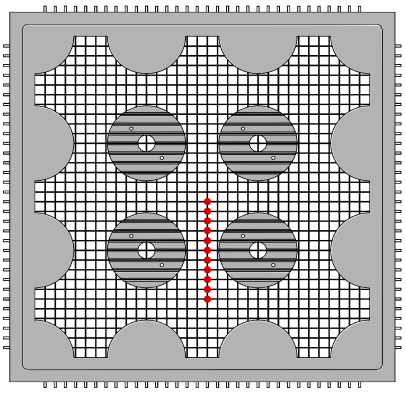

Figure 5.8: The red dots are used for evaluating the results of the rod-bundle. They are numbered 1 to 11, starting at the bottom.

The rod-bundle axial flow has several 'regions of interest' for computing the flow characteristics. If there are coherent structures in the flow, they would most likely form on the interface between the subchannel and a gap. This interface is not strictly determined because of the tapering shape of the rods. Furthermore the region around the gap is not fully symmetric, because there is a wall on one side and 'free flow' on the other side. Considering these two conditions, the red dots in figure 5.8 were selected as relevant points for computing the flow characteristics. They are numbered 1 to 11, starting at the dot closest to the wall. In a real application of the rod-bundle geometry, the bundle would consist of more rods and it would be sufficient to only take points from the center of a gap to the center of a subchannel into account.

Table 5.1: Physical properties of the flow in rod-bundle.

Re	U_{av} (m/s)	f	τ_w (Pa)	u_τ (m/s)
750	1.95×10^{-2}	2.1×10^{-2}	4.1×10^{-3}	2.0×10^{-3}
1500	3.95×10^{-2}	1.1×10^{-2}	8.3×10^{-3}	2.9×10^{-3}
3000	7.90×10^{-2}	1.1×10^{-2}	3.3×10^{-2}	5.8×10^{-3}
4500	1.19×10^{-1}	9.6×10^{-3}	6.8×10^{-2}	8.3×10^{-3}
6000	1.58×10^{-1}	9.0×10^{-3}	1.1×10^{-1}	1.1×10^{-2}

Scalar spectral density

If there are any coherent structures in the flow, they should be visible in the power spectrum, regardless of the physical mechanism behind it. As an example, we can take a look at the results from Adrian on large scale structures in turbulent flows in figure 2.2. The structures are visible in the spectrum as broad peaks, indicated with an arrow. Structures in the rod-bundle should show up in a similar way.

In figures 5.9, 5.10, 5.11, 5.12 and 5.13 the scalar power spectral densities of all the measurements are plotted. To make variations in the magnitude of the spectrum more visible, the spectra are plotted on a linear scale. In order to plot the spectra of several pixels of one measurement in a single graph, the spectra are plotted with an offset with respect to each other. The spectra are normalized, such that the area under the spectra is 1.

Examining the spectra in closer detail there are several notable features. First, there is a peak in all the pre-multiplied spectra between dimensionless wave-number $\kappa R = 2$ and $\kappa R = 4$, corresponding to a wavelength of 3 to 6 cm. This peak is not visible in the normal spectra, but by the nature of the pre-multiplied spectrum it becomes visible there. This way of plotting enlarges the spectrum at the intermediate wave-numbers, making the variation in that interval more visible. The peak goes to smaller wave-numbers, when moving closer to the center of the gap at pixel 6. However, the spectrum around the center of the gap is not symmetric. The spectra at the center subchannel generate a peak at a higher wave-number than the subchannel on the wall side. A possible explanation is that there is an effect of the wall, suppressing the high frequencies. Another possible explanation is that the tracer was not injected exactly in the middle of the gap, but a bit more to the side of the central subchannel. The presence of more tracer-fluid could lead to measurements with relatively more high frequent variations in the concentration than in the measurements at the 'wall side' of the gap. In an infinite rod-bundle geometry this difference in the location of the peak in the subchannels should not be there from the argument of symmetry. So, in any case, it is due to an imperfection in the experimental method and not inherent to the physical phenomena of the flow in a rod-bundle.

Second, the formation of an other peak, visible in both the normal as in the pre-multiplied spectrum, at higher Reynolds numbers can be noticed. When going to a turbulent flow a second peak starts to form around dimensionless wave-number $\kappa R = 0.3$, corresponding to a wavelength of 0.4 m. The peak becomes first visible at $Re = 3000$ and becomes more clear at the higher Reynolds numbers $Re = 4500$ and $Re = 6000$. The wave-number of the peak seems to be independent of the location of the pixel, however, the magnitude is not always equal. In the measurement at $Re = 4500$, the peak is more clear at the wall side of the gap, whereas at $Re = 6000$ the peak is more clear at the center subchannel side. The reason for that is yet unclear. It could be due to imperfections in the experimental method, but there can be a physical explanation as well. It could for example be that structures form in the rod-bundle in a organized way, always on the same side of the gap throughout the entire geometry.

Summarizing, the power spectral densities show that there are structures in the flow. There always are structures of 3 to 6 cm present, but turbulence introduces a new large scale structures of 40 cm which are more frequently present at higher Reynolds numbers. The exact physical mechanism for the formation of the structures is not yet known.

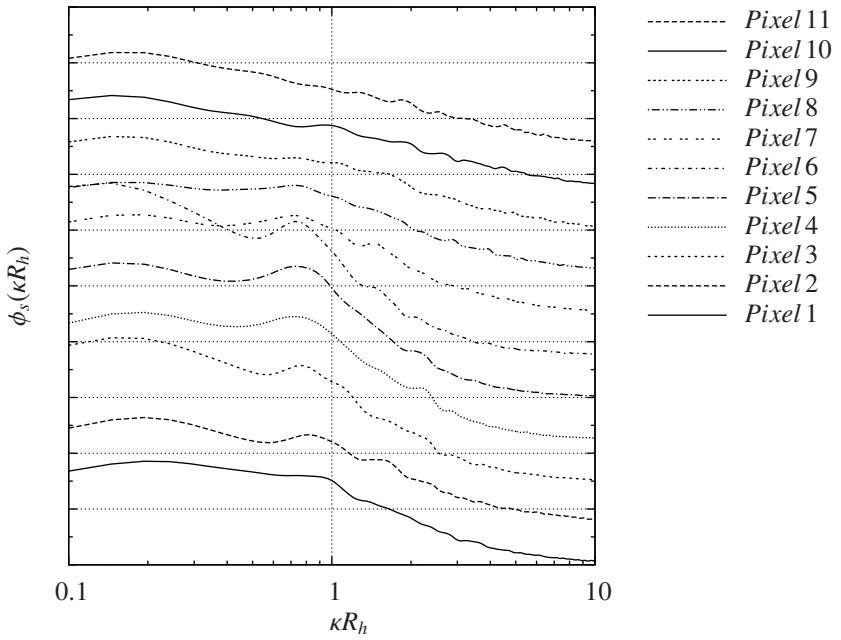

(a) Power spectral density at $Re = 750$

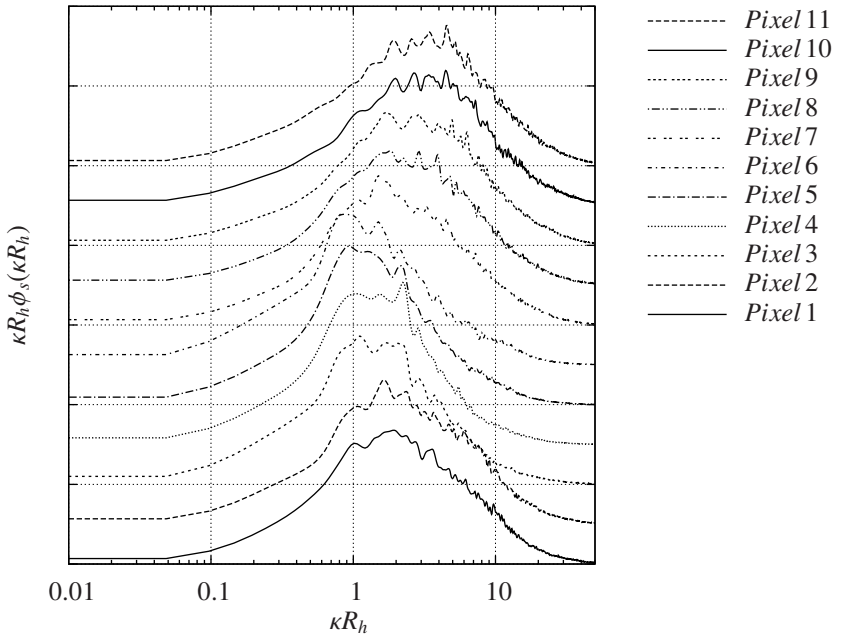

(b) Pre-multiplied power spectral density at $Re = 750$

Figure 5.9: The power spectral density at $Re = 750$. The spectra are plotted with an offset with respect to each other. The areas under the spectra are normalized to 1.

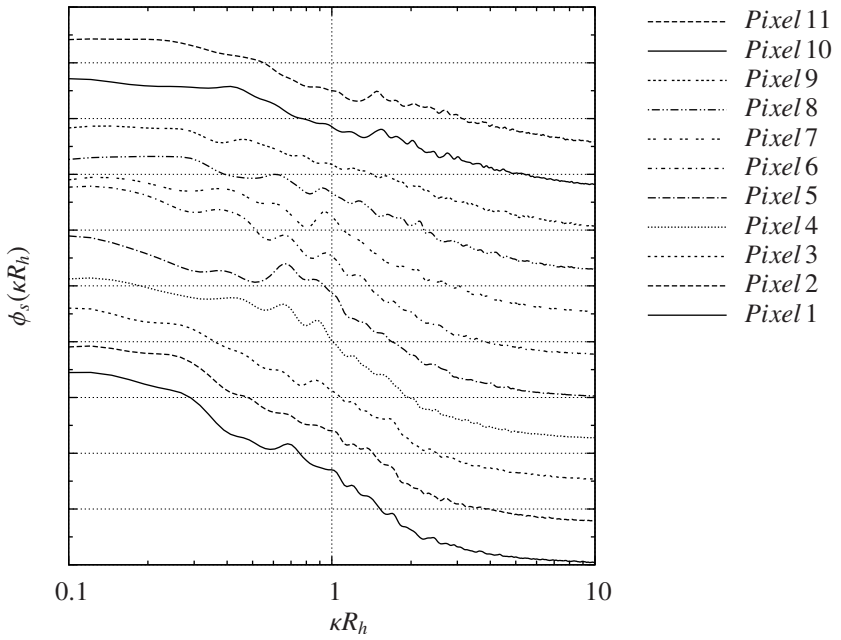

(a) Power spectral density at $Re = 1500$

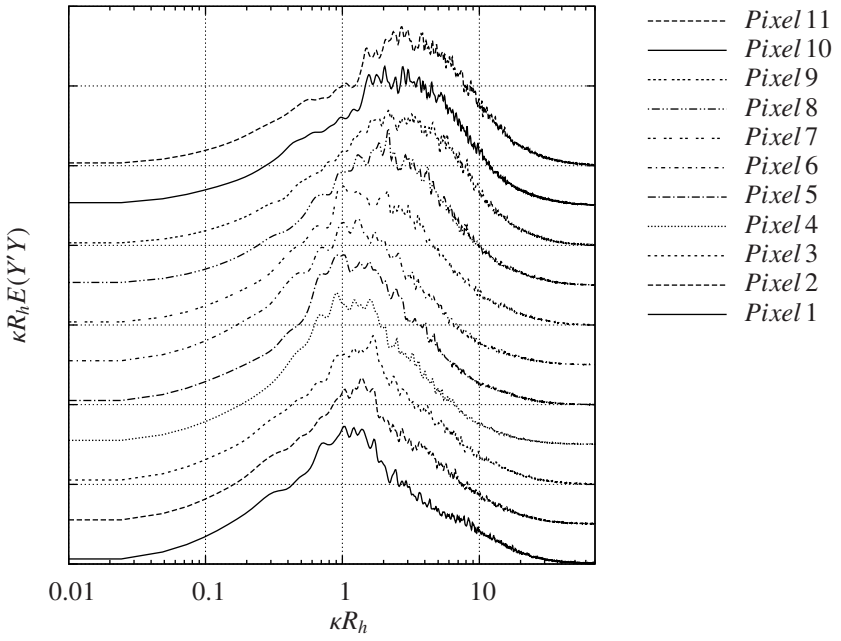

(b) Pre-multiplied power spectral density at $Re = 1500$

Figure 5.10: The power spectral density at $Re = 1500$. The spectra are plotted with an offset with respect to each other. The areas under the spectra are normalized to 1.

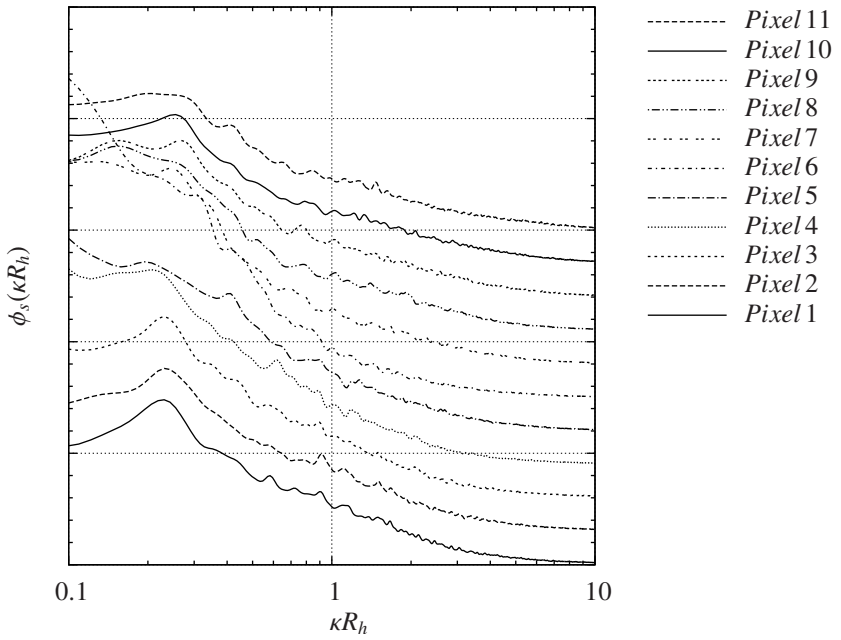

(a) Power spectral density at $Re = 3000$

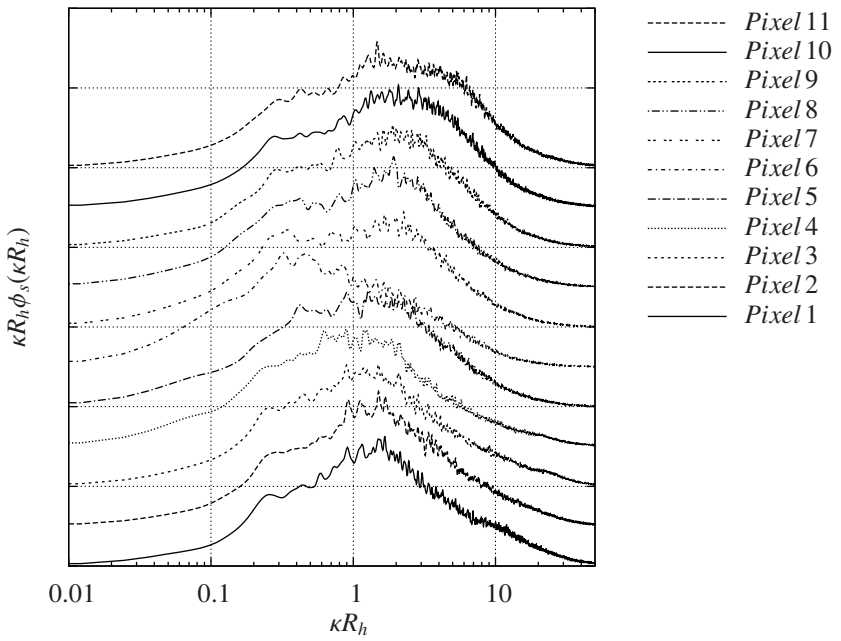

(b) Pre-multiplied power spectral density at $Re = 3000$

Figure 5.11: The power spectral density at $Re = 3000$. The spectra are plotted with an offset with respect to each other. The areas under the spectra are normalized to 1.

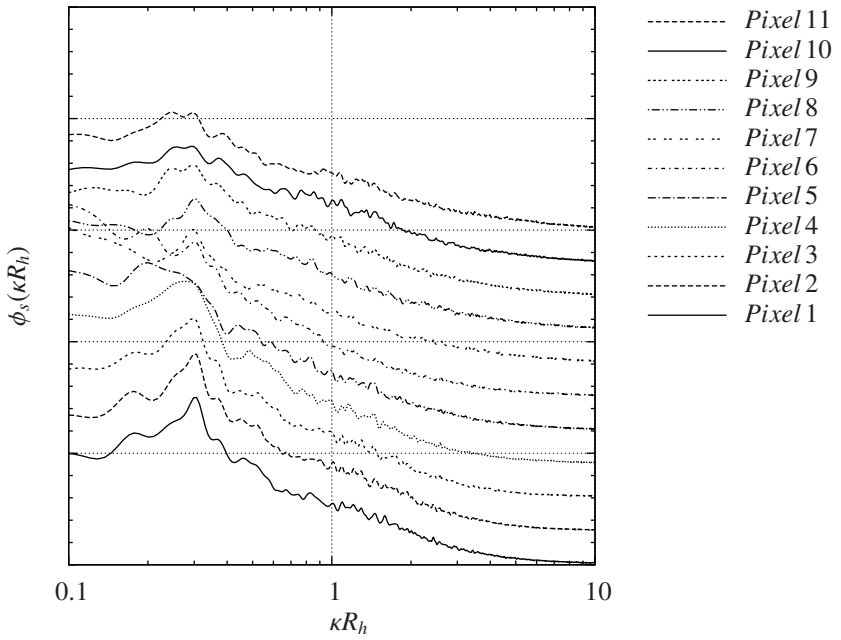

(a) Power spectral density at $Re = 4500$

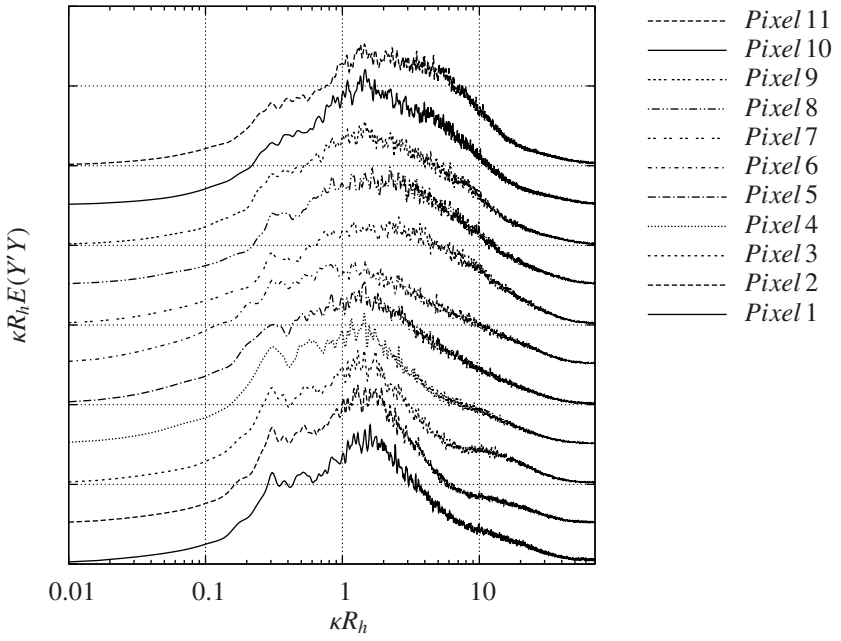

(b) Pre-multiplied power spectral density at $Re = 4500$

Figure 5.12: The power spectral density at $Re = 4500$. The spectra are plotted with an offset with respect to each other. The areas under the spectra are normalized to 1.

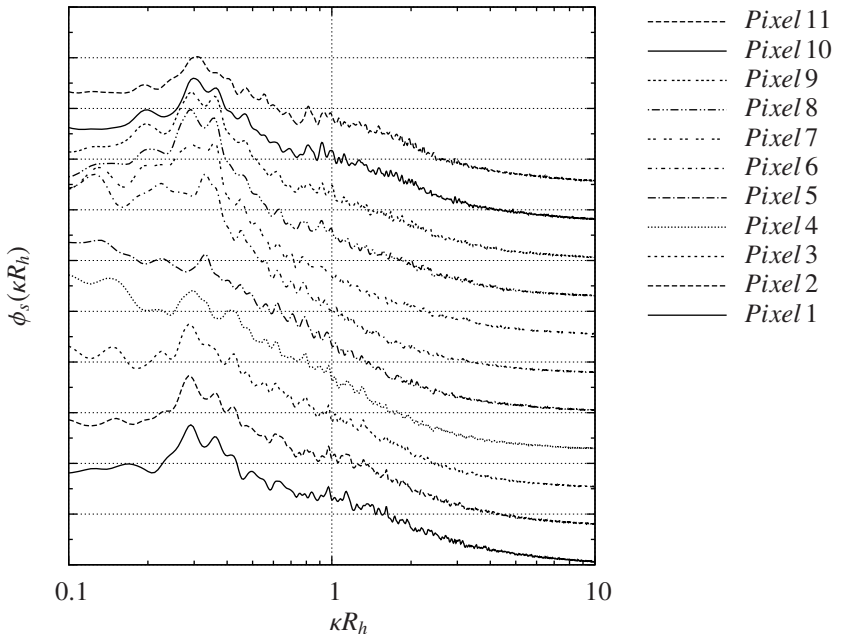

(a) Power spectral density at $Re = 6000$

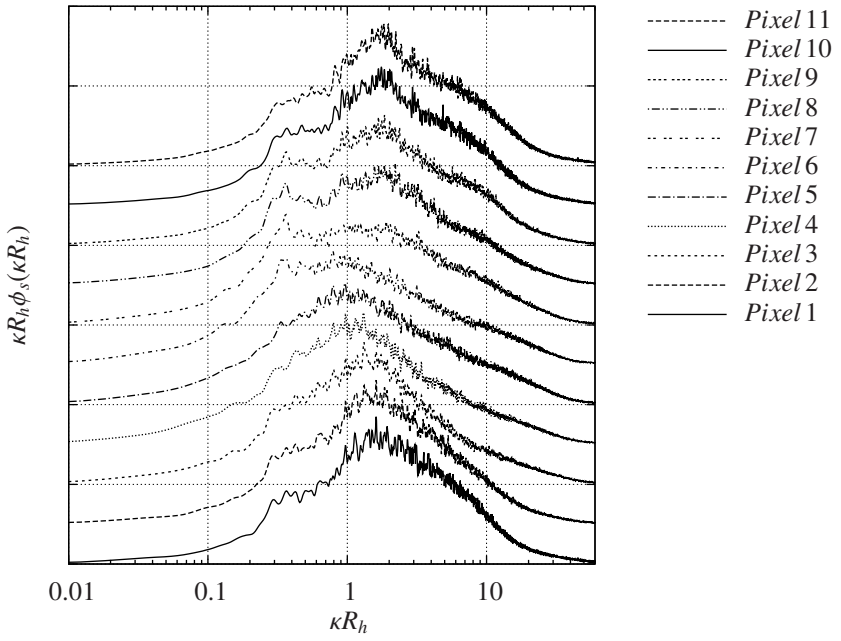

(b) Pre-multiplied power spectral density at $Re = 6000$

Figure 5.13: The power spectral density at $Re = 6000$. The spectra are plotted with an offset with respect to each other. The areas under the spectra are normalized to 1.

Multi-point correlation

To get a better understanding on the characteristics of the structures in the flow, the cross-correlation can be computed. In figure 5.14 the cross-correlation of pixel 9 with every other pixel is plotted at different time-lag for a laminar and a turbulent flow. The black line indicates the center of the gap between the rods. Using the average velocity the time-lag is converted to a distance. As already explained in section 4.2, the correlation drops very fast over a short range; to make the correlations of larger structures visible the color range is adjusted.

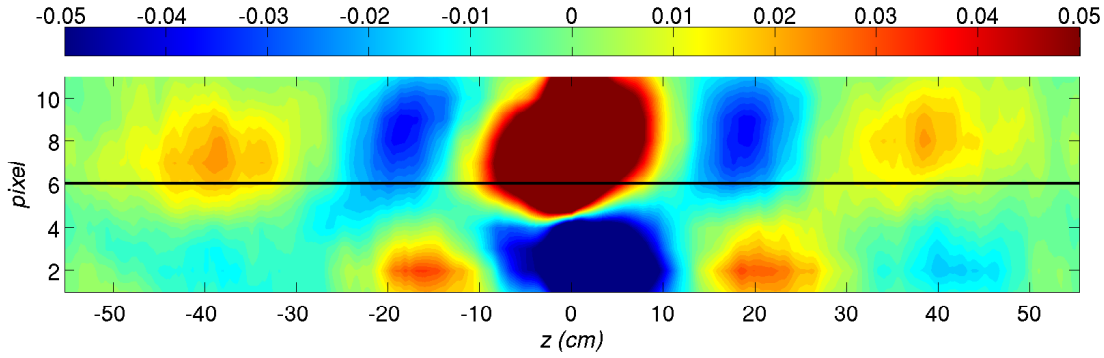

(a) $Re = 6000$

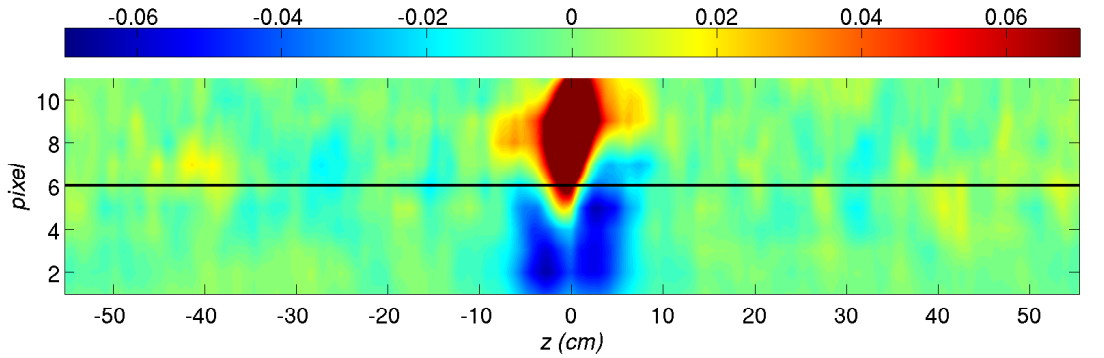

(b) $Re = 1500$

Figure 5.14: The cross-correlation at Reynolds numbers 6000 and 1500 of pixel 9 with every other pixel at different time shift. The time-shift is converted to distance using the average velocity. The black line indicates the center of the gap.

The correlation of the $Re = 6000$ flow shows a clear pattern of crosswise minima and maxima. This indicates a structure that is moving back and forward in an oscillating manner between the two subchannels, passing through the gap. When defining the structure size as the distance between two minima or maxima in the streamwise direction, a size 0.4 m, around 10 times the hydraulic diameter, is found. This coincides with the findings of the power spectrum. There is a clear distinction between the correlation in the turbulent flow and in the laminar flow. The flow of $Re = 1500$ does not show any correlation over large distances in the flow. There is negative correlation between the two sides of the gap in a diagonal manner, so out of phase in time, as can be seen by the two blue blobs. This is an indication of a structure that moves trough the gap, but in a different way as the structure in the turbulent flow. The structure is a single diagonal motion through the gap instead of a repetitive oscillation. Looking at the structure length in the streamwise direction it can be noticed that any correlation disappears in about 6 cm, so in the order of the hydraulic diameter; this matches with the results from the power spectral density too. The other laminar flow, with $Re = 750$, shows a similar behavior as the $Re = 1500$ flow. It is chosen to present the $Re = 1500$ flow, because the result of the $Re = 750$ flow was less clear. The flows of $Re = 3000$ and $Re = 4500$ show similar correlations as the $Re = 6000$ flow. From the power spectrum, it

can be seen that the structures visible in the laminar flow are also present in the turbulent flow. However from picture of the cross-correlation of the $Re = 6000$ flow this is not clear, since the oscillating structure conceals any structure smaller than 10 cm. Apparently the oscillating structures dominates the flow, making the smaller structures invisible in the multi-point correlation-function.

Flow visualization
The wire-mesh sensor has probes evenly distributed over the entire cross section of the flow. This makes it possible to generate pictures of the flow and to do visual inspections of the flow structures. These could help in getting a better understanding of the flow characteristics and is potentially a good addition on the information obtained from statistical methods like the power spectral density and correlation functions. In figure 5.15 the flows of Reynolds number $Re = 750$ and $Re = 6000$ from the rod-bundle, together with the $Re = 41\,000$ from the pipe flow, are visualized for both the same time and the same equivalent distance. Figure 5.15a, 5.15b and 5.15c show the flows for a time interval of 20 seconds, figure 5.15d, 5.15e and 5.15f show the flows for a fluid column of 1 m. The visualization of the rod-bundle flows is done along the line of the pixels indicates in figure 5.8, but for more pixels. The black lines represent the edge of the rods next to the gap, they coincide with pixel 2 and 10. The pipe flow visualization is done for a line over the entire diameter of the pipe. The visualization of the flow is in the basis only a qualitative method to get some better understanding to the structure and dynamics of a flow; nevertheless, some attempts are made to match the flow visualizations with other results.

The $Re = 750$ flow in figure 5.15d shows a column of tracer-fluid, with some protrusions at the sides. They seem to appear on one side of the gap, and then, with some delay, on the other side. For example there are two of these structures between the 8 m- and the 8.1 m mark, implying a size of a couple of centimeters. This coincide with the structure size found with the power spectrum. The multi-point cross-correlation predicted a time lag between the concentration on the sides of the gap, this is also confirmed by the visualization.

The $Re = 6000$ flow in figure 5.15b also shows the protrusions at the side, but in a more regular manner. The time lag in the correlation function in figure 5.14a is disappeared, however the structures that apparently cause this correlation are still there. A possible explanation is that other structures dominate the flow, probably turbulent structures. Two more motions can be detected. One is fast irregular motion in the form of small spikes on the side of the tracer column, this is probably due to the turbulence. The other motion is a large-scale oscillation between the two sides of the gap. Zooming in on the flow with figure 5.15e this oscillation can be seen clearly between the 42.6 m and the 43 m mark. This length-scale coincides with the peak in the power spectrum that shows up for turbulent flows.

Comparing the turbulent rod-bundle axial flow with the turbulent pipe flow the following things can be noticed. The pipe flow shows a central column of tracer-fluid with some structure bulging out on the sides. These structures show similarities with the protrusions in the rod-bundle flows. Furthermore, it can be noticed that in the pipe flow, the tracer-fluid moves a lot through the pipe. This is the reason why the concentration of tracer-fluid sometimes seems to go to 0. In figure 5.15f at the 77 s mark the movement of the tracer moves can be observed, since it moves along the line of the image. This wandering around of the fluid is a clear difference with the rod-bundle geometry. In the pipe, the fluid has a lot of freedom to perform any motion. In the gap of the rod-bundle geometry the fluid is constricted in its movement, bringing more order and regularity in the motions and inducing certain structures in the fluid. Whether these structures are Kelvin-Helmholtz like structures or caused by an other mechanism is not clear.

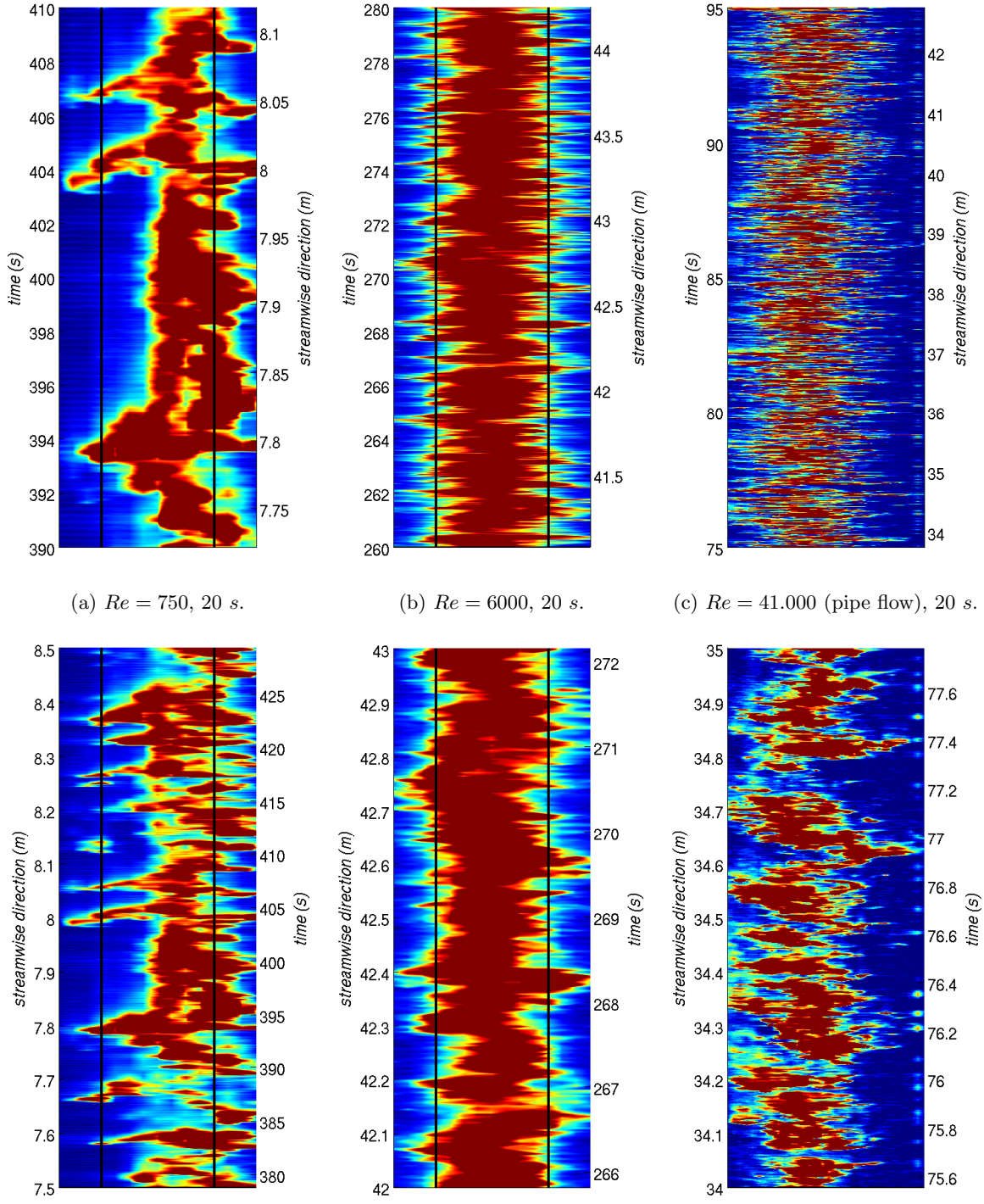

(a) $Re = 750$, 20 s. (b) $Re = 6000$, 20 s. (c) $Re = 41.000$ (pipe flow), 20 s.

(d) $Re = 750$, 1 m. (e) $Re = 6000$, 1 m. (f) $Re = 41.000$ (pipe flow), 1 m.

Figure 5.15: A plot of the tracer concentration through a part of the cross-section of the rod-bundle geometry along the red dots in figure 5.8, compared with the concentration at the diameter in the pipe flow. The black lines represent the edges of a rod, the center channel is on the right side. The images from the rod-bundle are generated at 50 Hz, the pipe flow image at 300 Hz.

cross-correlation

Passive-scalar measurement gives no information on the velocity of the flow. In order to still be able to measure this, Prasser [24] suggested a setup of two closely spaced wire-meshes. By maximizing the cross-correlation (equation 4.8) between the time-series of the two wire-meshes, an attempt was made to reconstruct the velocity. The time-lag at the maximum correlation is in theory the time that it took the tracer to be transported from one wire-mesh to the other. The results were checked with an LDA measurement. In a real flow the reconstruction of the velocity turned out the be unreliable, but for determining the average velocity it was a good method. Because the rod-bundle set-up has two wire-meshes, it is possible to apply this method.

As an example for a typical cross-correlation function the correlation of pixel 7 with its overlying pixel in the other wire-mesh sensor in the $Re = 6000$ flow, is plotted in figure 5.16. Is shows that the correlation is at it's maximum at 0.205 s, which corresponds to a velocity of 0.195 m/s. This is 22% higher than the average velocity. The velocity determined with the cross-correlation method always turned out to be much higher than the average velocity. In turbulent flow from 20% higher in the gap up to 40% higher in the center of the channel and in laminar flows from 30% higher in the gap up to 50% higher in the center of the channel. By manually checking the time-series at random for different individual peaks in the time-series of two overlying pixels, similar results were obtained. The only physical explanation for this is a very-steep gradient in the streamwise velocity throughout the cross section of the rod-bundle geometry.

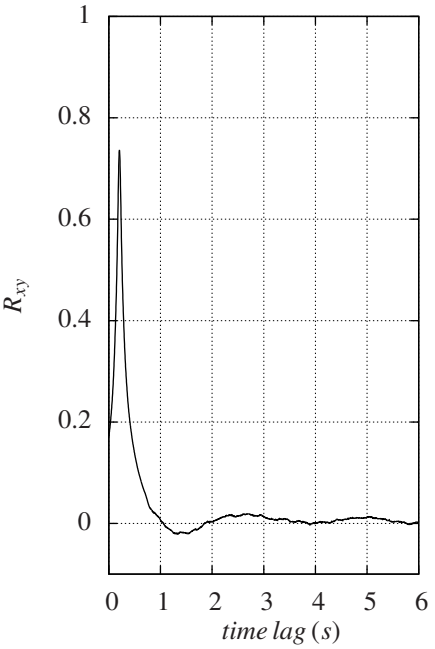

Figure 5.16: The cross-correlation function between pixel 7 and the the overlying pixel in the other mesh.

One-point correlation

In order to determine the presence of coherent structures, the auto-correlation can be used too. A large coherent structure, like the ones that are expected to be present in the rod-bundle geometry, will give several peaks in the auto-correlation function. We will define the structure size as the distance between 0 and the first maximum. In figure 5.17 the auto-correlation of pixel 9 for the Reynolds numbers 750, 3000 and 6000 are plotted. This pixel at these particular Reynolds numbers was chosen in order to compare the results with the findings of Bulk. He found structures of 12 cm, 18 cm and 30 cm for the Reynolds numbers 750, 3000 and 7000 respectively. The auto-correlation of this study shows structures of 40 cm at $Re = 6000$, 50 cm at $Re = 3000$ and no large scale structures at $Re = 750$. This is in agreement with the findings from power spectral density. The $Re = 3000$ has a maximum between 30 and 50 cm, depending on the pixel, which could indicate that this flow is in some sort of transitional state where the presence of large-scale structures is weaker.

The findings of Bulk and this current research are not in agreement. Also the findings of Mahmood [5] and Van Campen [6] show very different results as can be seen in figure 5.18. Their results show the presence of large-scale structures at low Reynolds numbers and a decreasing size of the structures for larger Reynolds numbers. This research only finds large scale structures at the larger Reynolds numbers and with a size that is, almost, independent of the Reynolds number.

The difference with the results from Bulk can be explained by the fact that Bulk computed the auto-correlation with single, short measurements, what can result in large variance in the results. The results from Van Campen were obtained from the same rod-bundle geometry, but with a different measurement section. A possible explanation for the different results could be the quality of the set-up. Because it is made from PVC, it is very vulnerable for vibrations and mechanical forces. Van Campen found that this was a limiting factor in the quality of his results too. When doing measurements of the secundairy flow in the rod-bundle flow, he found a flow that was an order of magnitude larger than what was to be expected from the theory.

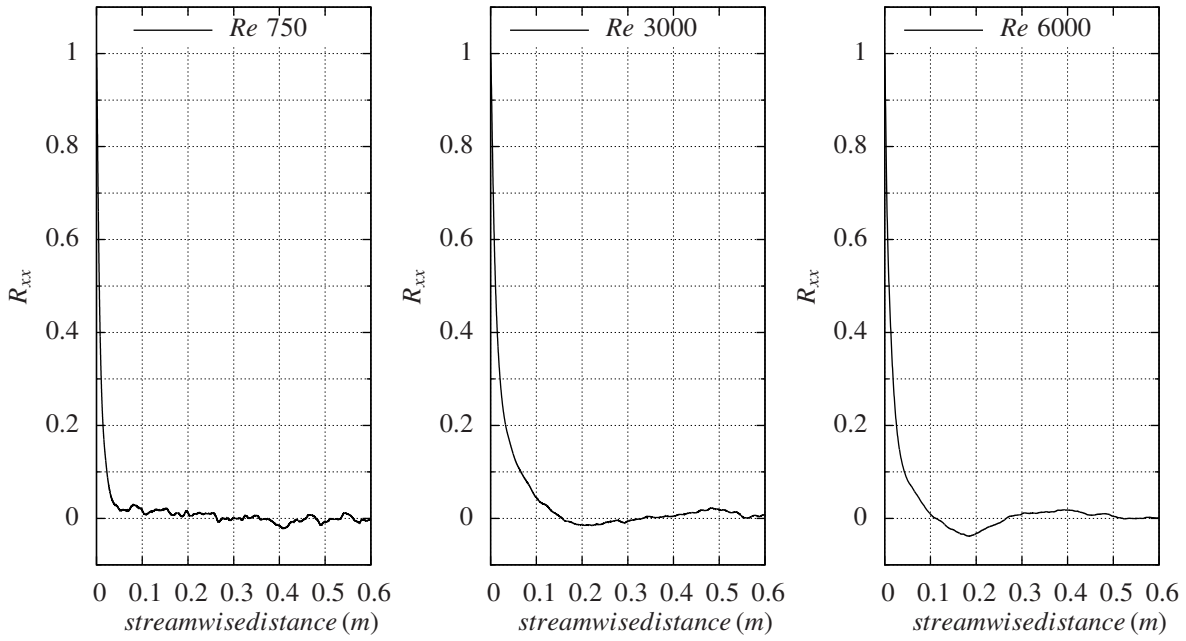

(a) $Re = 750$ (b) $Re = 3000$ (c) $Re = 6000$

Figure 5.17: The auto-correlation of pixel 9 for the Reynolds numbers 750, 3000 and 6000.

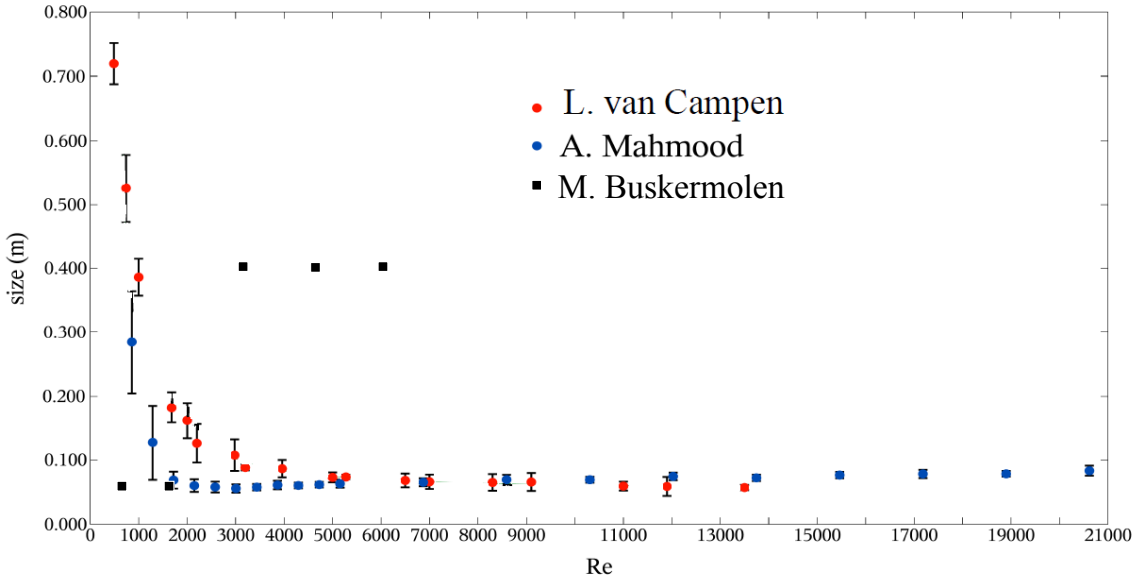

Figure 5.18: Structure size a function of the Reynolds number as found by Mahmood and Van Campen. The measurements of Mahmood were in a different geometry.

5.4 Conclusions on the rod-bundle axial flow

Based on the measurements with the wire-mesh sensor in the rod-bundle axial flow, the following conclusions can be made. These conclusions are a quick summary of the results, a more extensive discussion can be found in chapter 6.

On the passive-scalar measurement technique using a wire-mesh sensor

- *The wire-mesh sensor can be used to visualize the flow using a passive scalar as tracer*: The flow structure of a line in the cross-section can be examined over time.
- *It is possible, when using two wire-mesh senors on close distance, to determine the local average velocity using a cross-correlation function*: Although possible, the reliability has to be determined yet.
- *Multi-dimensional cross-correlation functions can be made using a wire-mesh sensor*: By calculating the cross-correlation of one pixel with all other pixels a two-dimensional picture can be made by applying Taylor's hypothesis.

On passive-scalar measurements in a rod-bundle axial flow at Reynolds numbers 750, 1500, 3000, 4500 and 6000

- *In a laminar flow structures with a size between 3 and 6 cm form, which is in the order of the hydraulic diameter*: This follows from the power spectral density and the multi-point cross-correlation.
- *In turbulent flow, additional large-scale coherent structures with a size of* 40 *cm form, this is in the order of 10 hydraulic diameters*: This is determined from the power spectral density and the multi-point cross-correlation.
- *The large-scale coherent structures perform a oscillating motion between the subchannels*: Using the multi-point cross-correlation this was determined.
- *The rod-bundle axial flow shows a more regular mixing profile, compared to the pipe flow*: The flow visualization indicates that the rod-bundle geometry constricts the fluid in it's movement.
- *The results from this research show significant differences with the results from Bulk and Van Campen*: This research shows small structures in the laminar flow and large-scale structures in the turbulent flows, whereas Bulk and Van Campen structures that decreased in size for higher Reynolds numbers.

Chapter 6

Conclusions

In this research, the technique of passive-scalar measurement using a wire-mesh sensor was improved. It was successfully applied to a pipe flow and to a rod-bundle axial flow. The wire-mesh sensor has the advantage that it has probes throughout a cross-section of the flow geometry. This makes it an interesting device for measurements in geometries that have limited optical access.

From the results, the following conclusions can be made.

Passive-scalar measurement using a wire-mesh sensor.
In previous research, the wire-mesh sensor was used for the measurement of a passive scalar successfully, but the correlation functions and power spectral densities, suffered from high variance. In this research, this variance was reduced by using the following techniques:

- Ensemble averaging. Using the fact that the flow is statistically stationary, the results of N data sets can be averaged. The variance is reduced by a factor of $\sqrt{N}$. The square-root dependency limits the practical use of this method, because the reduction of variance becomes less per sample, as the number of samples increases. It was found that in practice 10 to 20 measurement sets are useful.
- Welch Overlapped Signal Averaging (WOSA); a method of calculating the power spectral density. The WOSA method cuts the time-series of a measurement in equal pieces and calculates the power spectral density for every piece using a extended periodogram. Next, the power spectrum of the whole measurement set is made by averaging the spectra of the individual pieces. Spectral leakage is prevented by making the pieces overlap. The length of the pieces needs to be longer than the longest wavelength present in the signal.

Besides the variance reduction in the correlation functions and power spectral densities, in this research other techniques to evaluate the physical properties of a flow were also implemented in the wire-mesh sensor.

- Using Taylor's hypothesis the time-series made by the wire-mesh sensor can be transformed into spatial series. This makes it possible to determine the cross-correlation function in three dimensions in space, by calculating the cross-correlation function of a single pixel with every other pixel. Such a three-dimensional cross-correlation can be used to determine the shape and size of structures in the flow.
- Also using Taylor's hypothesis, a flow visualization can be made by using a two-dimensional picture of the time-series of a line of pixels. When transforming the time-series into a spatial series, a sort of snap-shot of a plane in the flow can be constructed. Such a visualization can be used as a qualitative means of determining the flow structure, which can be a helpful tool when interpreting the results of statistical evaluations, like power spectra and correlation functions.

- The probability density function of the fluctuations of a passive scalar can be calculated from the time-series of the pixels of the wire-mesh sensor. Here too, because the wire-mesh sensor has multiple probes, the PDF of the scalar fluctuations can be determined throughout the cross-section of a plane in a single measurement.

- The local average-velocity can be determined using two wire-mesh sensors, placed at a close distance from each other. In order to calculate the velocity, the time-shift that maximizes the cross-correlation between two overlying pixels has to be determined. It is unclear to what extent this method is reliable.

Measurements in a pipe flow
To check whether passive-scalar measurements using the wire-mesh sensor produced reliable results, measurements were done in pipe flow. This flow geometry is intensively studied, which makes it a suitable candidate for comparison with other research.

In a horizontal, gravity-driven pipe flow ensemble measurements were done at Reynolds numbers 18 000 and 41 000. A solution of ordinary kitchen salt was used as a passive scalar, and the measurements were done using only one wire-mesh sensor. The power spectrum of the passive scalar was considered to be fully-developed after 10 pipe diameters from the injection point. The power spectrum for the $Re = 41\ 000$ flow shows κ^{-1} dependency. This is in agreement with the results of Nye and Brodkey [33]. The power spectrum of the $Re = 18\ 000$ flow has a $\kappa^{-0.8}$ dependency, hence a slightly different spectrum than the $Re = 41\ 000$ flow. Because measurements were done at only two Reynolds numbers, it is not possible to say if the spectrum develops to a κ^{-1} dependency from the Reynolds number 18 000 to 41 000. Furthermore, since the spatial resolution of the wire-mesh is low compared to the smallest eddies in the flow, it also is not possible to say whether the $Re = 18\ 000$ has a κ^{-1} at higher wave-numbers. No research was found of passive-scalar spectra in the core of a pipe at Reynolds numbers around 20 000 in order to validate the results of the $Re = 18\ 000$ flow. A $\kappa^{-\frac{5}{3}}$ dependency was not found, which would have indicated the existence of an inertial subrange according to the eddy break-up model. This probably means that the flow is not isotropic turbulent, which is not a surprise, since the assumption of isotropic turbulence is only valid for very high Reynolds numbers. Also, the flow was wall-bounded whereas the isotropic turbulence model assumes an unbounded flow.

From the auto-correlation function, it was determined that both the $Re = 18\ 000$ flow and the $Re = 41000$ flow have an average structure size of 7 cm in the streamwise direction, this in the order of the pipe diameter. A two-dimensional cross-correlation function was calculated to determine the average shape of the structures in the flow. For both Reynolds numbers, an elongated shape was found. Since the flow is bounded by the wall, the growth of structures is limited in the radial direction, so an elongated shape is expected. The correlation function of the $Re = 41\ 000$ flow has a negative part, indicating the presence more complicated structures, for example, counter-rotating swirls. Such counter-moving structures are known to cause negative correlations.

To examine the mixing of tracer-fluid through the pipe a radial dispersion measurement was performed for the $Re = 41\ 000$ flow. A Gaussian distribution was found in the radial direction, which is in agreement with measurements from Lee and Brodkey [35], and is supported by Taylor's theory of turbulent dispersion.

A probability density function of the concentration fluctuations showed a high kurtosis for fluctuations over small distances. The kurtosis decreased to a value of 11 for larger distances. This decrease in kurtosis from small to large distances is found in the simulations of Chen and Kraichnan [36] too. Qualitatively, this verifies the PDF determined with the wire-mesh sensor. However, the simulations of Chen and Kraichnan were made in a isotropic flow and the kurtosis converged to a value of 4, which corresponds to a Gaussian PDF. This support the findings of the power spectral density that the assumption of isotropic turbulence is not valid for the core of the pipe flow we consider.

Measurements in a rod-bundle axial flow
In order to determine the presence of large-scale coherent structures in a rod-bundle axial flow, passive-

scalar measurements were done using a wire-mesh sensor. This flow geometry is a good example of a geometry that is hard to access with optical measurement techniques.
The flow was a vertical and gravity driven, with a pitch-to-diameter ratio of 1.4. The set-up had two wire-mesh sensors, in order to be able to determine the local average-velocity. Measurements were done at the Reynolds numbers 750, 1500, 3000, 4500 and 6000.

From the power spectrum and pre-multiplied power spectrum, two types of structures were found. In the laminar flows structures with a size in the order of the hydraulic diameter were found. In the turbulent flows, both a structure with a size in the order of the hydraulic diameter, and a large-scale structure with a size in the order of 10 hydraulic diameters were found. For increasing Reynolds numbers, the large-scale structure becomes more dominant in the spectrum. The large-scale structure was found at the interface of the gap and the subchannel region. In the middle of the gap and in the middle of the subchannel, the large-scale structure was, at most, very weakly present. This can be an indication that, as predicted, a large shear-stress at the interface of the gap and the subchannel is the mechanism that forms the large-scale structure.

From the multi-dimensional cross-correlation function it was found that the 'laminar structure' has a negative correlation between two adjacent subchannels that is out of phase in time. This could indicate a structure that moves between two subchannels, through the gap, in a slanting manner. The multi-dimensional cross-correlation function for the turbulent flow shows a large-scale oscillating motion in the streamwise direction, with negative correlation between two adjacent subchannel, that is in phase in time. This could indicate a structure that moves back and forward trough the gap in some sort of clockwise manner.

By making a visualization of the flow structure, an attempt was made to give a qualitative analysis of the structures in the flow, for both laminar and turbulent flow. As a comparison, also a visualization of the pipe flow experiment was made. It showed that the gap-regions in the rod-bundle constrict the fluid in its motion, organizing it and making it less chaotic, when compared to a pipe flow. Although the Reynolds number in the pipe flow is almost an order of magnitude higher, it can be assumed that the dampening effect of the gap will still be there for higher Reynolds numbers in the rod-bundle flow, restricting the fluid its motion.

The local average-velocity could be determined by finding the time shift that maximizes the cross-correlation function of two overlying pixels in the two wire-mesh sensors. This velocity turned out the be $30 - 50\%$ higher than the average velocity. Because the reliability of this result is unknown, it was decided not to use these velocities in other results.

With the auto-correlation function, the existence of large-scale structures in turbulent flows was validated. The difference with respect to previous results, from both Bulk and Van Campen, was significant. Their results show large-scale structures for low Reynolds numbers and a decreasing structure size for larger Reynolds numbers, whereas this research found two structures, a small laminar structure and a large-scale turbulent structure.

Chapter 7

Recommendations

Based on the results from this research, the following recommendations can be done, both on improvements of the rod-bundle set-up and on recommendations for future research on passive-scalar measurement using a wire-mesh sensor. The goal of recommendations would be to get further insights in the physics of the pipe flow, in the mixing properties of the rod-bundle flow and to get insight in whether or not there are large-scale coherent structures in the rod-bundle axial flow.

Rod-bundle set-up

- *Use stiffer material for the rods*: The rods in the rod-bundle are made from pipe of PVC. This makes them very flexible and vulnerable for vibrations and mechanical stresses. Even though this set-up has a measurement section with stronger rods, still the effect of the plastic rod is unknown. In the research from Van Campen [6], the vibrations and deformations in the plastic caused secundairy flows of an order of magnitude larger than what was to be expected from the theory. When preparing the rod-bundle set-up for the wire-mesh sensor, the rods in the measurement section were fortified, but still the flexible plastic parts elsewhere in the set-up could be of influence of the flow properties. Further fortifications could prevent this.
- *Make the wire-mesh sensor easily accessible and use a filter*: Dust from the environment gets easily stuck in the wires from the wire-mesh sensor and every set-up with water is vulnerable for the growth of algae. A filter could prevent for dust and dirt to get in the system and it is highly recommendable to inspect and clean the wire-mesh sensor regularly.
- *Use a dedicated wire-mesh acquisition box*: The individual pixels in the wire-mesh sensor had different sensitivities and and had an offset from each other. In a gas liquid flow this is not a problem since the contrast between the two fluid is very high. In passive-scalar measurement it makes the calibration hard and it prevents from real concentration measurements. The software could be improved also, to allow for longer measurements at high frequency and to make data storage more efficient.

Future research

- *Do a velocity experiment in a pipe flow and construct the velocity profile in the rod-bundle geometry*: The reliability of the local-velocity calculations was unknown, which prevented from them from being used. Here, also the pipe flow can be used to validate results. The velocity profile of a pipe flow is well known, so by reconstructing this profile with two closely-spaced wire-mesh sensors, the reliability of the data can be determined.
- *Determine the scalar spectrum density in the center of a pipe flow over a large range of Reynolds numbers (10 000 - 250 000)*: The physical reason for the κ^{-1} dependency in the $Re = 41\ 000$ flow

is unknown. An experiment over a large range of Reynolds number could help to determine the physical mechanism.

- *Do passive-scalar measurements in the rod-bundle axial flow and in a pipe flow at similar Reynolds numbers*: In order to compare the structure of the flow of the rod-bundle axial flow and the pipe flow, measurements need to be done at similar Reynolds numbers.
- *Do a dispersion experiment in the rod-bundle geometry*: By doing such an experiment, a quantitative description of the mixing properties can be made. It can be checked if Taylor's dispersion theory applies to the rod-bundle geometry.
- *Determine the effect of vibrations of the rods*: The flexibility is of the rods seems to be a returning problem in the studies of the rod-bundle axial flow. Although stiffer rods could reduce vibrations, it would be useful to have an understanding of their contribution in the measurement results. By introducing controlled vibrations in the system, for example with small weight attachments on the rods, the effect of mechanical vibrations can be determined.
- *Develop a correction factor for the probe size of the wire-mesh sensor*: Such a correction factor could increase the frequency domain in which the wire-mesh sensor operates reliably.
- *Do simulations for the rod-bundle geometry*: Eventually, the results of the measurements of the dispersion,velocity, correlations functions and spectral densities should be used as a reference point in developing a model for the mixing between two subchannels.

Appendix A

Derivation of the $-\frac{5}{3}$ law

To derive the $\kappa^{-\frac{5}{3}}$ dependency of the energy spectrum in the inertial subrange, we must start with the Kolmogorov hypotheses for turbulent flows with high Reynolds number:

i. **Local isotropy:** The motions at the small scales, $\ell \ll \ell_0$, are statistically isotropic.

ii. **First similarity hypothesis:** The statistics of the small-scale motions $\ell < \ell_{EI}$ are uniquely defined by ν and ϵ.

iii. **Second similarity hypothesis:** The statistics of the motions of the scale in the range $\ell_0 \gg \ell \gg \eta$ are uniquely determined by ϵ and are independent of ν.

Next, we define the wavenumber κ according to equation A.1.

$$\kappa \equiv \frac{2\pi}{\ell} \tag{A.1}$$

Now, it is possible to define a energy spectrum function $E(\kappa)$ using the hypothesis of local isotropy. Since isotropy is assumed, the energy spectrum can be independent of the direction. Using the first similarity hypothesis, the function will be solely defined by κ, ν and ϵ. Writing the function in a non-dimensionalized form we obtain:

$$E(\kappa) = (\epsilon\nu^5)^{\frac{1}{4}}\phi(\kappa\eta) \tag{A.2}$$

If we now define the Kolmogorov velocity as in equation A.3.

$$u_\eta \equiv (\nu\epsilon)^{\frac{1}{4}} \tag{A.3}$$

Equation A.2 can be written as equation A.4.

$$E(\kappa) = u_\eta^2\eta\phi(\kappa\eta) \tag{A.4}$$

In which $\phi(\kappa\eta)$ is some non-dimensionalized function called the Kolmogorov spectrum function. If now ϵ and κ are used to non-dimensionalize the function instead, the following function is found.

$$E(\kappa) = \epsilon^{\frac{2}{3}}\kappa^{-\frac{5}{3}}\Psi(\kappa\eta) \tag{A.5}$$

In which $\Psi(\kappa\eta)$ is the compensated Kolmogorov spectrum function, related to $\phi(\kappa\eta)$ according to:

$$\Psi(\kappa\eta) = (\kappa\eta)^{\frac{5}{3}}\phi(\kappa\eta) \tag{A.6}$$

The second similarity hypothesis states that the energy spectrum function can be described independently of ν in the inertial subrange. The only place where ν can be found is in the argument of Ψ. When taking a closer look at this argurment, it can be seen that the hypotesis is only valid for $\kappa\eta \ll 1$, since $\kappa_{EI} < \kappa < \kappa_{DI}$. Hence, the hypothesis states that the function Ψ should be independent of its argument, when the argument is very small. Then, the energy spectrum becomes:

$$E(\kappa) = C\epsilon^{\frac{2}{3}}\kappa^{-\frac{5}{3}} \tag{A.7}$$

Appendix B

Derivation Kelvin-Helmholtz instabilities

The general derivation of K-H instabilties according to the book of Kundu [9] is as follows:

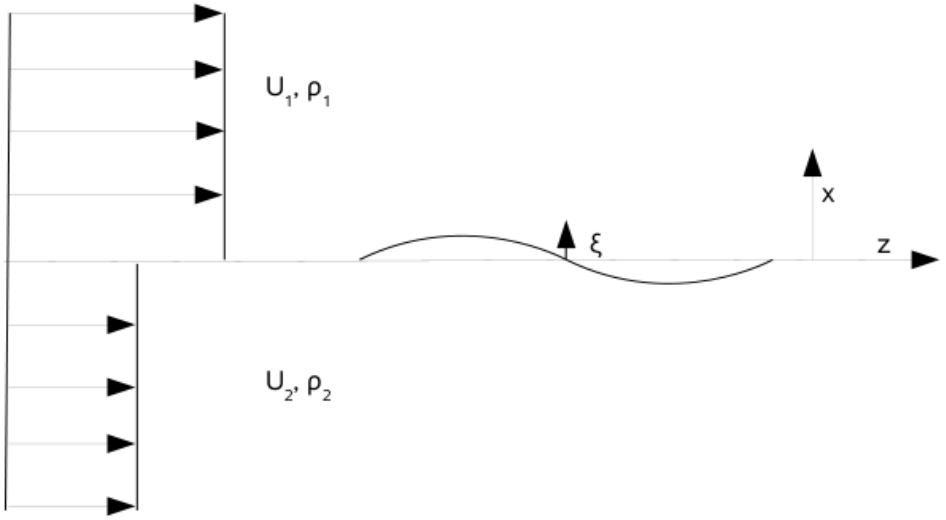

Figure B.1: A perturbed interface of a flow with a discontinuous velocity and density.

We start with an irrotational flow with two layers of fluid, each with a different uniform velocity U_1 and U_2 and density ρ_1 and ρ_2. The boundary between the layers is assumed to be infinitesimally small. Since in the rod-bundle problem the gravity is in the z-directions, hence tangential to the flow, gravitational effects will not be accounted for.

Next a small perturbation on the boundary layer is introduced as in figure B.1. Since the perturbation is small and the velocity is uniform in both layers, it is assumed that the flow can be described using a potential flow, satisfying for the perturbed flow:

$$\nabla^2\tilde{\phi}_1 = 0, \qquad \nabla^2\tilde{\phi}_2 = 0 \tag{B.1}$$

$$\tilde{\phi}_1 = U_1 z + \phi_1, \quad \tilde{\phi}_2 = U_2 z + \phi_2 \tag{B.2}$$

Substituting B.2 in B.1 gives the equations for the perturbations:

$$\nabla^2\phi_1 = 0, \qquad \nabla^2\phi_2 = 0 \tag{B.3}$$

With conditions:

$$\begin{aligned} \phi_1 &\to 0, \qquad \text{as } x \to \infty \\ \phi_2 &\to 0, \qquad \text{as } x \to -\infty \end{aligned} \tag{B.4}$$

The velocity needs to be continuous across the boundary layer. Therefore the solution of the perturbations needs to satisfy:

$$\begin{aligned} \frac{\partial \phi_1}{\partial x} &= \frac{\partial \chi}{\partial t} + U_1 \frac{\partial \chi}{\partial z}, \qquad \text{at } x = 0 \\ \frac{\partial \phi_2}{\partial x} &= \frac{\partial \chi}{\partial t} + U_2 \frac{\partial \chi}{\partial z}, \qquad \text{at } x = 0 \end{aligned} \tag{B.5}$$

Besides the velocity, also the pressure needs to be continuous at across the interface, so $p_1 = p_2$ at $x = \chi$. To achieve this, Bernoulli equation can be used:

$$\begin{aligned} \frac{\partial \tilde{\phi}_1}{\partial t} + \frac{1}{2}(\nabla^2 \tilde{\phi}_1)^2 + \frac{\tilde{p}_1}{\rho_1} &= C_1 \\ \frac{\partial \tilde{\phi}_2}{\partial t} + \frac{1}{2}(\nabla^2 \tilde{\phi}_2)^2 + \frac{\tilde{p}_2}{\rho_2} &= C_2 \end{aligned} \tag{B.6}$$

In the unperturbed state these equations, using equation B.1, lead to the following condition:

$$\rho_1 \left(\frac{U_1^2}{2} - C_1 \right) = \rho_2 \left(\frac{U_2^2}{2} - C_2 \right) \tag{B.7}$$

Now using equation B.2 to fill in equation B.6 and requiring $p_1 = p_2$ at $x = \chi$, we obtain:

$$\begin{aligned} \rho_1 C_1 - \rho_1 \frac{\partial \phi_1}{\partial t} - \frac{\rho_1}{2} \left[(U_1 + u_1)^2 + v_1^2 + w_1^2 \right] \\ = \rho_2 C_2 - \rho_2 \frac{\partial \phi_2}{\partial t} - \frac{\rho_2}{2} \left[(U_2 + u_2)^2 + v_2^2 + w_2^2 \right] \end{aligned} \tag{B.8}$$

To find an equation for the perturbation, the condition for the unperturbed state given in equation B.8 can be subtracted and non-linear terms are ignored.

$$\rho_1 \left[\frac{\partial \phi_1}{\partial t} + U_1 \frac{\partial \phi_1}{\partial x} \right]_{x=0} = \rho_2 \left[\frac{\partial \phi_2}{\partial t} + U_2 \frac{\partial \phi_2}{\partial x} \right]_{x=0} \tag{B.9}$$

Now a solutions has to be found for the perturbation that satisfies the conditions given in equations B.3, B.4, B.5 and B.9. A good candidate to start with is a normal mode of the form:

$$(\chi, \phi_1, \phi 2) = (\hat{\chi}, \hat{\phi_1}, \hat{\phi} 2) e^{ik(z - ct)} \tag{B.10}$$

in which k is real and c is a complex number with form $c = c_r + c_i$. This solution is stable as long as c only has a real part, when c becomes complex, the solution becomes unstable.
When this normal mode is substituted in the Laplace equation B.3 together with condition B.4, the general solutions for the perturbations are found:

$$\begin{aligned} \hat{\phi}_1 &= A e^{-kx} \\ \hat{\phi}_2 &= B e^{kx} \end{aligned} \tag{B.11}$$

To solve A and B, the condition B.5 can be used:

$$\begin{aligned} A &= -i(U_1 - c)\chi \\ B &= i(U_2 - c)\chi \end{aligned} \tag{B.12}$$

Substituting these conditions together with the general solution given in equation B.11, a general solution for c can be derived:

$$c = \frac{\rho_2 U_2 + \rho_1 U_1}{\rho_2 + \rho_1} \pm \left[-\rho_1 \rho_2 \left(\frac{U_1 - U_2}{\rho_1 + \rho_2} \right)^2 \right]^{\frac{1}{2}} \tag{B.13}$$

If now is taken into account that inside a rod-bundle geometry the fluid is homogeneous, so $\rho_1 = \rho_2$, the specific c for our problem is found:

$$c = \frac{1}{2}(U_1 + U_2) \pm \frac{i}{2}(U_1 - U_2) \tag{B.14}$$

Since there always is a complex part in c, the solution is unstable and perturbations will grow into instabilities as in figure 5.2.

Bibliography

[1] D. E. Coates, "Interchannel mixing and cooling temperature distribution in seven and nineteen element fuel bundles," *Canadian General Electric Company Ltd. X07-10001R*, 1960.

[2] J. T. Rogers and N. E. Todreas, "Coolant interchannel mixing in reactor fuel rod bundles single-phase coolants," in *ASME Annual Winter Meeting, New York, U.S.A.*, 1968.

[3] D. S. Rowe, B. M. Johnson, and J. G. Knudsen, "Implications concerning rod bundle crossflow mixing based on measurements of turbulent flow structure," *International Journal of Heat and Mass Transfer*, vol. 17, no. 3, pp. 407 – 419, 1974.

[4] K. Rehme, "The structure of turbulence in rod bundles and the implications on natural mixing between the subchannels," *International Journal of Heat and Mass Transfer*, vol. 35, no. 2, pp. 567 – 581, 1992.

[5] A. Mahmood, *Single-phase crossflow mixing in a vertical tube bundle geometry.* PhD thesis, Delft University of Technology, Delft, 2011.

[6] L. J. A. M. van Campen, "An experimental investigation on the use of fep as refractive index matching material for lda in a rod bundle flow," Master's thesis, Delft University of Technology, Delft, 2009.

[7] A. Ylönen, W.-M. Bissels, and H.-M. Prasser, "Single-phase cross-mixing measurements in a 4× 4 rod bundle," *Nuclear Engineering and Design*, vol. 241, no. 7, pp. 2484–2493, 2011.

[8] F. P. Bulk, "An experimental study on cross-flow mixing in a rod-bundle geometry using a wire-mesh," Master's thesis, Delft University of Technology, Delft, 2012.

[9] P. K. Kundu and I. M. Cohen, *Fluid Mechanics.* Academic Press, 2nd ed., 2002.

[10] S. B. Pope, *Turbulent flows.* Cambridge university press, 2000.

[11] K. C. Kim and R. J. Adrian, "Very large-scale motion in the outer layer," *Physics of Fluids (1994-present)*, vol. 11, no. 2, pp. 417–422, 1999.

[12] M. Guala, S. E. Hommema, and R. J. Adrian, "Large-scale and very-large-scale motions in turbulent pipe flow," *Journal of Fluid Mechanics*, vol. 554, p. 521, 2006.

[13] X. Wu, J. R. Baltzer, and R. J. Adrian, "Direct numerical simulation of a 30 r long turbulent pipe flow at $r_+ = 685$: large- and very large-scale motions," *Journal of Fluid Mechanics*, vol. 698, pp. 235–281, 2012.

[14] J. R. Baltzer, R. J. Adrian, and X. Wu, "Structural organization of large and very large scales in turbulent pipe flow simulation," *Journal of Fluid Mechanics*, vol. 720, pp. 236–279, 2013.

[15] L. Fulachier and R. Dumas, "Spectral analogy between temperature and velocity fluctuations in a turbulent boundary layer," *Journal of Fluid Mechanics*, vol. 77, no. 2, pp. 257–277, 1976.

[16] G. K. Batchelor *et al.*, "Small-scale variation of convected quantities like temperature in turbulent fluid," *J. Fluid Mech*, vol. 5, no. 1, pp. 113–133, 1959.

[17] H.-M. Prasser, A. Böttger, and J. Zschau, "A new electrode-mesh tomograph for gas–liquid flows," *Flow Measurement and Instrumentation*, vol. 9, no. 2, pp. 111–119, 1998.

[18] P. T. M. Smeets, "Spatially resolved phase distributions in a vertical gas-liquid-liquid flow," Master's thesis, Delft University of Technology, Delft, 2007.

[19] C. Walker, M. Simiano, R. Zboray, and H.-M. Prasser, "Investigations on mixing phenomena in single-phase flow in a t-junction geometry," *Nuclear Engineering and Design*, vol. 239, no. 1, pp. 116–126, 2009.

[20] H.-M. Prasser, D. Scholz, and C. Zippe, "Bubble size measurement using wire-mesh sensors," *Flow measurement and Instrumentation*, vol. 12, no. 4, pp. 299–312, 2001.

[21] H.-M. Prasser, E. Krepper, and D. Lucas, "Evolution of the two-phase flow in a vertical tube—decomposition of gas fraction profiles according to bubble size classes using wire-mesh sensors," *International Journal of Thermal Sciences*, vol. 41, no. 1, pp. 17–28, 2002.

[22] H.-M. Prasser, J. Zschau, D. Peters, G. Pietzsch, W. Taubert, and M. Trepte, "Fast wire-mesh sensors for gas-liquid flows-visualisation with up to 10 000 frames per second," tech. rep., American Nuclear Society, 555 North Kensington Avenue, La Grange Park, IL 60526 (United States), 2002.

[23] H. Pietruske and H.-M. Prasser, "Wire-mesh sensors for high-resolving two-phase flow studies at high pressures and temperatures," *Flow measurement and instrumentation*, vol. 18, no. 2, pp. 87–94, 2007.

[24] H.-M. Prasser, "Generalixed cross-correlation technineqe for the measurement of time-dependent velocities," in *The 15th International Topical Meeting on Nuclear Reactor Thermal - Hydraulics*, 2013.

[25] A. Manera, *Experimental and analytical investigations on flashing-induced instabilities in natural circulation two-phase systems*. PhD thesis, Delft University of Technology, 2003.

[26] M. N. Descamps, *Experimental study of three-phase gas-lift*. PhD thesis, Delft University of Technology, 2007.

[27] R. J. Belt, *On the liquid film in inclined annular flow*. PhD thesis, Delft University of Technology, 2007.

[28] L. J. A. M. van Campen, *Bulk dynamics of droplets in liquid-liquid axial cyclones*. PhD thesis, Delft University of Technology, 2014.

[29] D. B. Percival and A. T. Walden, *Spectral analysis for physical applications: multitaper and conventional univariate techniques, 583 pp.* Cambridge Univ. Press, New York, 1993.

[30] D. J. Thomson, "Spectrum estimation and harmonic analysis," *Proceedings of the IEEE*, vol. 70, no. 9, pp. 1055–1096, 1982.

[31] L. P. B. M. Janssen and M. M. C. G. Warmoeskerken, *Transport Phenomena Data Companion*. Delft University Press, 2001.

[32] J. O. Hinze, "Turbulence," *New York*, 1959.

[33] J. O. Nye and R. S. Brodkey, "The scalar spectrum in the viscous-convective subrange," *Journal of Fluid Mechanics*, vol. 29, no. 01, pp. 151–163, 1967.

[34] M. S. Uberoi and L. S. G. Kovasznay, "Influence of resolving power on measurement of correlations and spectra of random fields.," 1951.

[35] J. Lee and R. S. Brodkey, "Turbulent motion and mixing in a pipe," *AIChE Journal*, vol. 10, no. 2, pp. 187–193, 1964.

[36] H. Chen, S. Chen, and R. H. Kraichnan, "Probability distribution of a stochastically advected scalar field," *Physical review letters*, vol. 63, no. 24, p. 2657, 1989.

[37] H. Tennekes and J. L. Lumley, *A First Course in Turbulence*. MIT Press, 1972.

[38] M. van Dyke, *An album of fluid motion*. Parabolic Press Stanford, 1982.

[39] T. Ikeno and T. Kajishima, "Analysis of dynamical flow structure in a square arrayed rod bundle," *Nuclear Engineering and Design*, vol. 240, no. 2, pp. 305–312, 2010.